

Numerical simulations of simultaneous pair-drop impacts and their energetics

Ziyao Zhang^{b,*}, Alfonso A. Castrejón-Pita^b, Wouter Mostert^b

^a*Department of Engineering Science, University of Oxford, Oxford, OX1 3PJ, United Kingdom*

Abstract

We present three-dimensional direct numerical simulations of the simultaneous impact of two identical drops on an hydrophobic substrate, varying the relative strength of capillary and viscous effects respectively through Weber and Reynolds numbers of impact. The interaction between the two drops is characterized by the appearance of a lamella arising from the collision of the two droplets' spreading rims. We examine the width, the height, and the general morphological evolution of the central sheet; the numerical data is validated against prior experiments and used to guide the development of an energetic model for the maximum elevation of the central sheet. In particular, the rise of the central sheet resembles the spreading behaviour single-drop impacts, especially at high Weber and Reynolds numbers. This fact can be used to estimate scalings in the capillary- and viscous-dominated regimes, which can be used to collapse the trajectories. These insights provide a route for a more complete understanding of the dynamics for the central rising sheet, and anticipate the detailed study of its fragmentation characteristics.

Keywords: pair droplets, simultaneous impact, central rising sheet

1. Introduction

Drop impact is a widespread and ubiquitous phenomenon in nature and industry. Ranging from rain in nature, which brings the smell of the earth [1], and furthermore causes the erosion of soil [2], drop impact is also important to applications in industry, such as inkjet printing, spray cooling, spray coating [3], continuous and pulsant impacts on turbine blade [4], and blood-splatter analysis [5]. Understanding this process and its underlying mechanisms advances our knowledge of natural physics, and facilitates its controlled application in industrial settings.

While it is necessary first to understand the impact of single drops, it is not unusual that in many industrial settings multiple drop impacts may occur in close proximity, such as in spray coating, inkjet printing, etc. [3, 6]. Such impacts should not be considered as a simple superposition of individual drop impacts because they may interact with one another. The inter-drop spacing Δx and time lag Δt between the two drops complicate this process, and generally simultaneous impacts, non-simultaneous impacts, or successive impacts can occur. For example, experimental and numerical work has been devoted to investigating successive impact and coalescence of drops while varying some of these parameters [7–10].

When two drops are separated by a certain Δx , falling at low speed, they interact with each other upon impact, coalesce, and then form a large film[11, 12]. When the drops fall at

*Corresponding author

Email address: ziyao.zhang@eng.ox.ac.uk (Ziyao Zhang)

high kinetic energy, their spreading lamellae collide at the midpoint between the two drops and form an additional, vertical sheet of liquid. Barnes et al. [13] investigated the simultaneous and non-simultaneous impact on a small target through a monodisperse apparatus. It was found that the drops ejected from the central sheet were 50% larger than those from single drop fragmentation. They also found that this 'splashing' behavior could occur at lower values of the splashing parameter K , than for single-drop impact, where K is defined as $K = We^{1/2}Re^{1/4}$, where We is Weber number and Re is Reynolds number. Roisman et al. [14] also studied pair-drop impacts on a dry substrate, and showed that the maximum height of the central sheet increased with decreasing Δx . They also defined a dynamic model for the maximum height of the central sheet, with an explicit solution given for simultaneous impact. Afterward, Liang et al. [15] and Gultekin et al. [16], in an experimental study, showed agreement with previous results and demonstrated that the maximum rising sheet height would increase with We . Gultekin et al. [16] compared their results with the theoretical solution given by Roisman et al. [14] but found disagreement in the case where the substrate was raised to an increased temperature. Ersoy and Eslamian [17] investigated the geometry and irregular splashing phenomenon of the central sheet, but faced challenges in their experiments in accounting for non-simultaneous drop impact. As in their experiments, the two drops impacted on the substrate within an inevitable time lag of 1 ms. Most recently, Goswami and Hardalupas [18] studied simultaneous pair-drop impact on a dry substrate. They experimentally showed the height evolution of the central sheet with respect to different impact velocities and inter-drop spacing, and empirically found that the maximum height scaled as $H_{s,max} \sim We_{L,imp}^{0.48}$, where $We_{L,imp}$ is the Weber number associated with the impact between the two spreading lamellae.

While previous studies have shed light on the interaction between two pair drops, the majority have used experiment, in which it is difficult, for example, to achieve precisely simultaneous impact of the pair drops. Numerical analysis can support an analysis of the problem not only by introducing precise control over impact parameters (see e.g. [19, 20]), but also complete information on the flow fields in the liquid and gas phases with high spatiotemporal phases. The main purpose of this study is twofold: Firstly, to reproduce the problem of simultaneous pair-drop impact in high-resolution three-dimensional (3D) numerical simulations, validated against available experimental data; and secondly, to use the resulting numerical data propose an energetic model for the maximum height of the central uprising sheet. The study proceeds as follows. In § 2, the physical and mathematical models are described first, and the numerical methods are explained and validated against experimental data. In § 3, we present our results: we first describe the whole process of pair-drop impacts; we present the effects of We , Re on the issue, including maximum spreading radius, central sheet width, its height, and overall morphology. In § 4, we propose a novel energetic model to explain the scaling law of the height as well as certain asymptotic behaviours of the height of the central sheet. Based on the analysis of scalings from energetic models, we obtain scaling laws for the maximum height of the central sheet and also the evolution time. We conclude in § 5 with remarks on future work.

2. Formulation and methodology

2.1. Mathematical and physical description

We consider the simultaneous pair-drop impact problem. The problem formulation is shown in Fig. S1, with dimensional variables indicated by carets. Two drops of diameter \hat{D}_0 with the same density $\hat{\rho}_l$, viscosity $\hat{\mu}_l$, and surface tension $\hat{\sigma}$ to ambient air are considered to impact on a substrate with velocity \hat{U}_0 and lateral separation $\Delta\hat{x}$; they are contained in a gas of density and

viscosity $\hat{\rho}_g, \hat{\mu}_g$. Gravitational acceleration \hat{g} is included in these simulations but its effect on the dynamics of the impact and droplet interaction is negligible. In simulations, a domain width of $16\hat{D}_0$ is chosen to minimize the effects of the domain boundary [21, 22], and the two drops are separated by $\Delta\hat{x} = 1.8\hat{D}_0$, which is mostly fixed in this study. We consider a simultaneous impact problem, where the two drops are initialized at the same vertical position to avoid any deformation of the drops due to air drag prior to impact [18]. Lateral and upper computational boundaries are set with outflow boundary conditions. The bottom computational boundary follows a non-slip velocity boundary condition, and we consider a hydrophobic surface here, namely the static contact angle $\theta_s = 90^\circ$.

The continuity and Navier-Stokes equation with surface tension for two-phase, viscous, immiscible flows can be written as [23–26]:

$$\frac{\partial\hat{\rho}}{\partial\hat{t}} + \nabla \cdot (\hat{\rho}\hat{\mathbf{U}}) = 0 \quad (1)$$

$$\hat{\rho} \left(\frac{\partial\hat{\mathbf{U}}}{\partial\hat{t}} + \hat{\mathbf{U}} \cdot \nabla \hat{\mathbf{U}} \right) = -\nabla\hat{p} + \nabla \cdot \left[\hat{\mu} \left(\nabla\hat{\mathbf{U}} + \nabla\hat{\mathbf{U}}^T \right) \right] + \hat{\sigma}\hat{\kappa}\delta_s\mathbf{n} + \hat{\rho}\hat{\mathbf{g}} \quad (2)$$

$$\nabla \cdot \hat{\mathbf{U}} = 0 \quad (3)$$

which describe the conservation of mass and momentum. Here $\hat{\mathbf{U}}$ is the velocity vector, \hat{p} is the fluid pressure, $\hat{\kappa}$ is the local curvature of the interface, \mathbf{n} is the normal vector at the interface, and δ_s is Dirac delta function which is nonzero only at the interface of two different fluids [27]. One can use the characteristic length \hat{D}_0 , velocity \hat{U}_0 , time \hat{D}_0/\hat{U}_0 to get the dimensionless system (the dimensional variables are with carets, dimensionless are not), and thus the parameter space can be described in terms of four non-dimensional numbers [2, 26]:

$$We = \frac{\hat{\rho}_l\hat{D}_0\hat{U}_0^2}{\hat{\sigma}}, \quad Re = \frac{\hat{\rho}_l\hat{D}_0\hat{U}_0}{\hat{\mu}_l}, \quad \rho_r = \frac{\hat{\rho}_l}{\hat{\rho}_g}, \quad \mu_r = \frac{\hat{\mu}_l}{\hat{\mu}_g} \quad (4)$$

which respectively describe the ratios of inertial and capillary effects, of inertial and viscous effects, and of density and viscosity between liquid and gas phases. For the purpose of comparison to the experimental setup of Goswami and Hardalupas [18] and Goswami [28], we will consider density and viscosity ratios relevant for water and 40% glycerol-water mixtures, in air, namely $\rho_r = 813$, $\mu_r = 56$ and $\rho_r = 910$, $\mu_r = 269$, respectively. For the values of $We \in [15, 200]$, $Re \in [938, 8000]$ considered in this study, we have verified that gravity does not have an appreciable role. The remaining details of the parameter space are shown in the Supplementary.

2.2. Numerical methods

The open-source package *Basilisk* is used to solve the nonlinear Navier-Stokes (NS) equations (1)–(3) with an octree-based adaptive mesh refinement (AMR) method, which retains an accurate description of the flow while providing considerable computational savings over uniform-mesh approaches [29]. The geometric volume-of-fluid (VOF) method is used in a momentum-conserving formulation for the advection and numerical reconstruction of the liquid-air interface, which minimizes the parasitic currents induced by surface tension [27]. The VOF tracer is advected according to [30]:

$$\frac{\partial f}{\partial\hat{t}} + \nabla \cdot (f\hat{\mathbf{U}}) = 0 \quad (5)$$

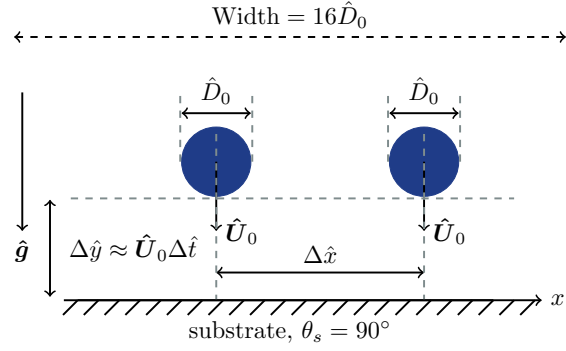


Figure 1: Problem formulation illustrated using a two-dimensional schematic. Carets denote dimensional variables throughout the figure

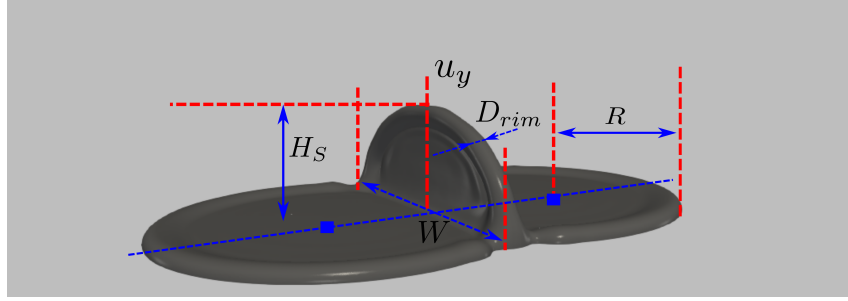


Figure 2: Definition of the measured variables of the central rising sheet formed by two drops after the second impact during the rising stage. The two blue squares indicate the assumed centers of the drops. D_{rim} , W , and H_s are defined as the corresponding maximum values

where f refers to the volume fraction to differentiate liquid and gas, and it follows that,

$$\begin{cases} f = 1 & \text{in the liquid phase,} \\ f = 0 & \text{in the gas phase,} \\ 0 < f < 1 & \text{in the interface.} \end{cases} \quad (6)$$

The density ρ and viscosity μ can then be expressed as:

$$\hat{\rho} = f\hat{\rho}_l + (1 - f)\hat{\rho}_g, \quad (7)$$

$$\hat{\mu} = f\hat{\mu}_l + (1 - f)\hat{\mu}_g. \quad (8)$$

The momentum equation is solved with the Bell-Colella-Glaz projection method [31], and viscous terms are solved implicitly. The VOF advection scheme is mass- and momentum-conserving by construction, and surface tension is modelled with an implementation of the continuum surface force model [30, 32]. Additional details can be found in Popinet [29, 30]. The minimum grid size used in the simulations is specified by $\Delta = 16\hat{D}_0/2^L$, where L is the maximum grid refinement level of AMR method. The results presented in this study are generally independent of mesh resolution at the chosen values of L ; see the Supplementary Information for further details. We present the notations of the central sheet in Figure 2 for following analyses.

3. Results

A basic overview of the process is shown in Figure 3; the right column shows snapshots from the numerical simulations and the left column shows snapshots taken at the same times from the

experiments of [18] for comparison, which is found to be broadly favourable between simulations and experiment in the following description. (Detailed comparisons are given below and in the Supplementary Material.) We begin by giving a coherent description of two-drop post-impact interaction. For the parameters shown, and generally in this study, the droplets do not splash after impact, and spread radially along the substrate each forming a lamella bordered by a rim. The droplets' lamellae collide initially at the centrepoint $x = y = z = 0$ at $0.4 < \tau < 0.5$ where $\tau \equiv \hat{t}\hat{U}_0/\hat{D}_0$, and the collision then proceeds symmetrically along the y axis in a "tank-treading" fashion. The collision results in the vertically rising lamella, which has a semilunar shape in the $z - y$ plane during the interaction. The central sheet is restrained by surface tension and reaches a maximum height before beginning to fall back to the bulk.

Figure 4 shows a quantitative comparison between experimental [18] and numerical results in terms of the maximum height of the central sheet, which is the focus of the study. The height of the central sheet as a function of time is $\hat{H}_s(\hat{t})$, which can be non-dimensionalised by $H_s \equiv \hat{H}_s/\hat{D}_0$. The comparison between numerics and experiment is good up to the maximum value $H_{s,max}$ which is attained at $\tau = \tau_{H_s}$. After this time, the results deviate for the pure water case (Figure 4a). In both experiments and in the present numerical simulations, these cases featured an unstable rim and occasional splashing; the disagreement between results may perhaps be attributed to differences in how the central sheet height is measured. But the agreement is significantly improved for the glycerol-water mixture ($\phi = 40\%$), which tend not to splash, at both the rising and falling stages. Therefore, the numerical platform can accurately and precisely capture both the dynamic features of central rising sheet and its geometric height when the corrugation in the rim of the central sheet are not strong. The discrepancies that do exist may be caused by several effects. Firstly, the simulations use a static contact angle, which is an idealisation of the dynamic contact angle in the experiment. Secondly, because the two reference experimental studies [18, 28] report slightly different initial drop diameters, there may be a small error incurred in matching Re within the numerical study. And thirdly, in experiment there are inevitable uncertainties in terms of impact time, inter-drop spacing, and drop morphology at impact moment. Some of these imperfections cause corrugations at the rising or falling stage or lead to the maximum height differences directly at all stages. Nevertheless, in the face of these differences, the numerical simulations are in excellent agreement with the experimental results.

3.1. Geometric considerations

We now consider the morphology of the pair-drop interaction in detail. Because the single-drop spreading on the substrates is well understood [2, 3, 33, 34], we are here especially interested in the central sheet height H_s , which characterises well the pair-drop interaction problem.

Now certain results from the literature on single-drop impacts are useful to provide a framework for understanding the pair-drop problem. In particular, the spreading behaviour of each drop on the side of the droplet opposite that of the interaction is relatively unchanged from the single-droplet case. Therefore we may consider the rim of the spreading lamella on the substrate to have radius \hat{R} as measured on this far side. The spreading ratio is the (equivalent) dimensionless spreading diameter $\beta = \hat{D}/\hat{D}_0$, where $\hat{D} = 2\hat{R}$. At the maximum extent of spreading, $\hat{R} = \hat{R}_{max}$ and $\beta_{max} = \hat{D}_{max}/\hat{D}_0$, and the central sheet reaches its maximum height at around the same time as maximum spreading (see below). Therefore β_{max} plays an important role in the central sheet in two ways: (1) increased β_{max} corresponds with a larger spreading time, which in turn allows for more of the total drop liquid to flow into the central sheet; and (2) it corresponds with a greater total width (W as shown in Fig. 2) of the central rising sheet.

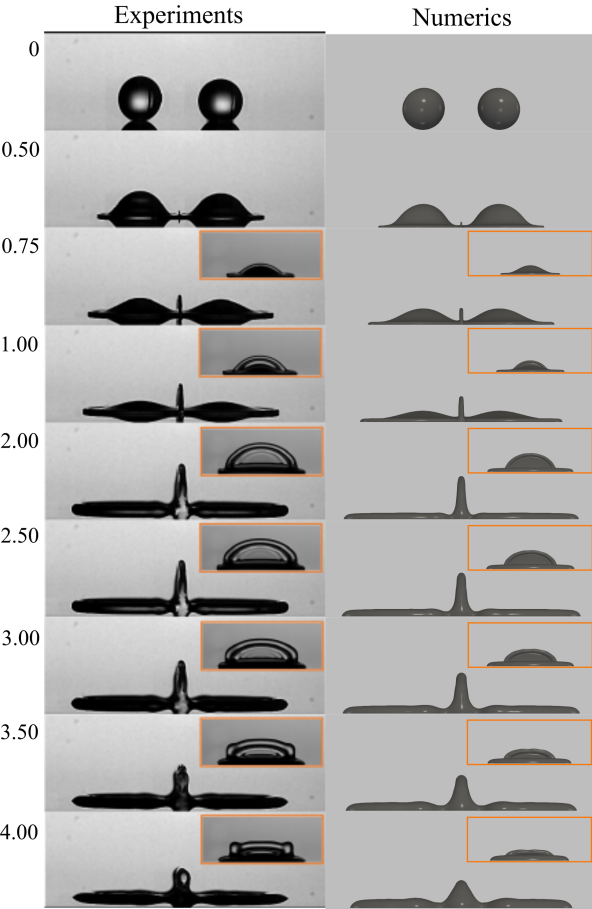


Figure 3: Comparison of the evolution of the central sheet with non-dimensional time τ between numerical simulations and experiments for $We = 130$ at $\phi = 40\%$ solution. Note: the experimental images are adapted from Goswami [28], CC BY 4.0

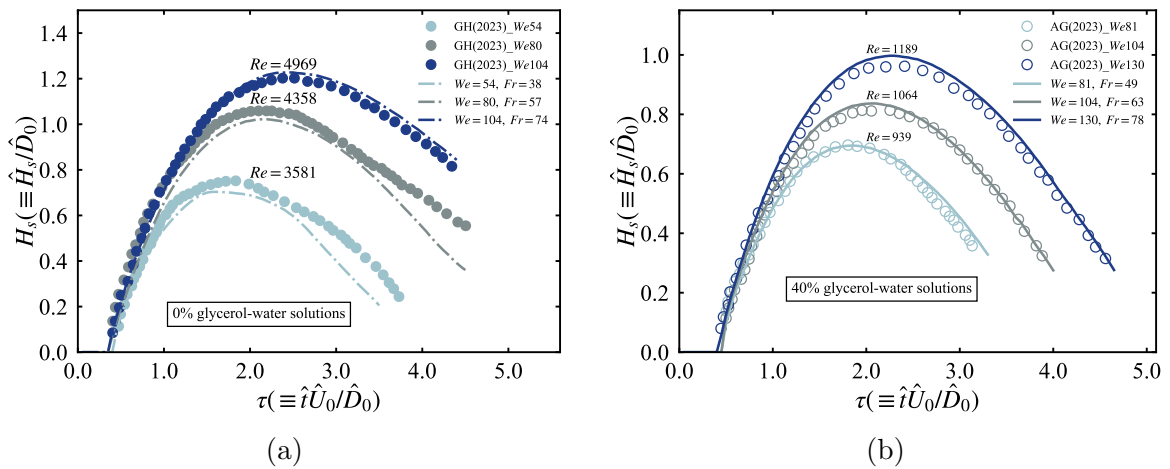


Figure 4: Comparison of the maximum heights between numerical results and experiments: (a) $\phi = 0\%$ solutions and (b) $\phi = 40\%$ solutions for three experimental cases with different We (the corresponding Re is obtained accordingly). Note: the experimental results are adapted from Goswami and Hardalupas [18]. For clarity, the definitions of variables are omitted from the labels in the following figures

It is desirable therefore to obtain an estimate of the maximum spreading ratio as a function of We , Re from the literature on single-drop impacts, which has variously considered both energetic and dynamic models [35–39] - see the Supplementary Information for a comparison. In short, our numerical data are in closest agreement with Wildeman et al. [36], whose theory will be used in the following development.

The evolution of β is compared with experiment, and as central sheets are also affected by the width W , the evolution of the width of central sheet under different We and Re are shown in Fig. 5. For β evolution, grey circles are data obtained from experiment [28], with which simulation results are again in good agreement. It is shown that β increases at first and then decreases after it reaches its maximum because the drops begin to retract. Because the width is confined by β_{max} and Δx geometrically, the trends of W roughly match those of β_{max} .

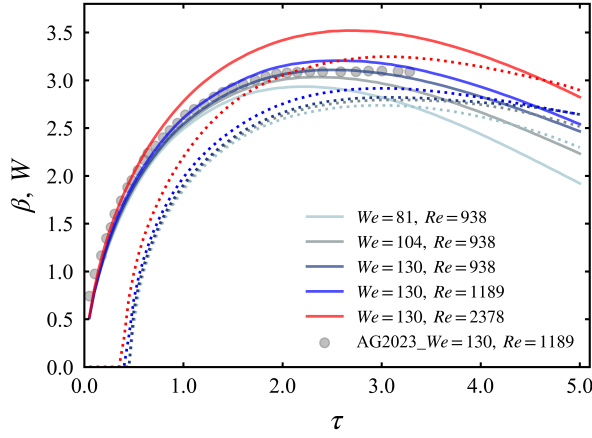


Figure 5: Evolution of the maximum spreading ratio $\beta \equiv D/D_0$, shown by solid lines, and the dimensionless width of the central interaction surface W , shown by dotted lines of the same color, for various We and Re . Reference experimental data adapted from Goswami and Hardalupas [18], are plotted as filled circles and show good agreement with the corresponding numerical results.

4. Energetics of the central rising sheet

Many studies focus on the energetics of single drop impacts [35, 36, 39, 40], but these are not fully understood for simultaneous pair-drop impacts. In this subsection, we investigate kinetic energy \hat{E}_k (KE), surface energy \hat{E}_s (SE), local viscous dissipation $\hat{\varepsilon}_d$, and total dissipation \hat{E}_d , which are expressed as [24, 36, 41]:

$$\hat{E}_k = \int_{\Omega} \frac{1}{2} \hat{\rho}_l (\hat{\mathbf{u}} \cdot \hat{\mathbf{u}}) \, d\Omega \quad (9)$$

$$\hat{E}_s = \int_{\hat{A}_{LV}} \hat{\sigma} \, d\hat{A}_{LV} - \int_{\hat{A}_{SL}} \hat{\sigma} \cos \theta_{eq} \, d\hat{A}_{SL} \quad (10)$$

$$\begin{aligned} \hat{\varepsilon}_d = & 2\hat{\mu} \left[\left(\frac{\partial \hat{u}_x}{\partial \hat{x}} \right)^2 + \left(\frac{\partial \hat{u}_y}{\partial \hat{x}} \right)^2 + \left(\frac{\partial \hat{u}_z}{\partial \hat{x}} \right)^2 \right] \\ & + \hat{\mu} \left[\left(\frac{\partial \hat{u}_x}{\partial \hat{y}} + \frac{\partial \hat{u}_y}{\partial \hat{x}} \right)^2 + \left(\frac{\partial \hat{u}_y}{\partial \hat{z}} + \frac{\partial \hat{u}_z}{\partial \hat{y}} \right)^2 + \left(\frac{\partial \hat{u}_z}{\partial \hat{x}} + \frac{\partial \hat{u}_x}{\partial \hat{z}} \right)^2 \right] \end{aligned} \quad (11)$$

$$\hat{E}_d = \int_0^{\hat{t}} \left(\int_{\Omega} \hat{\varepsilon}_d \, d\Omega \right) \, d\hat{t} \quad (12)$$

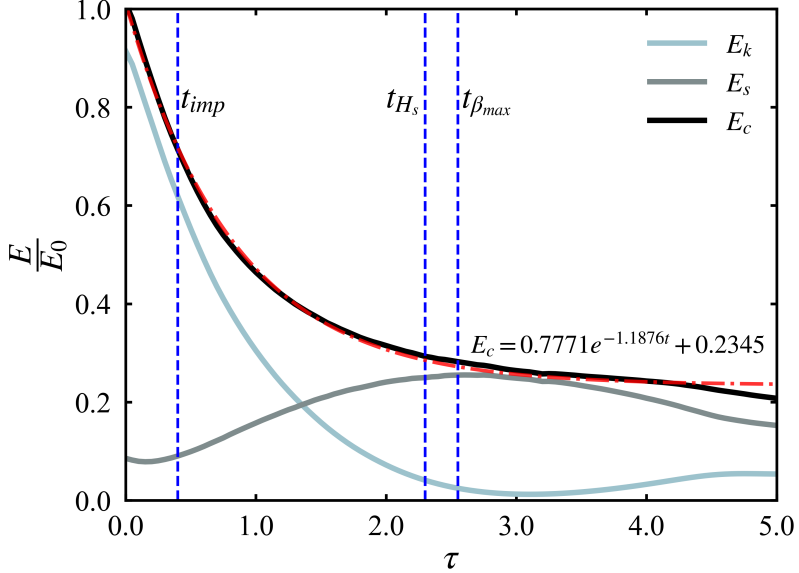


Figure 6: Evolution of the energy normalized by the initial total energy during the impact process for $We = 130$ and $Re = 1189$. Here, t_{imp} denotes the impact time, t_{Hs} the time of maximum sheet height, and $t_{\beta_{max}}$ the time at which the remaining drops on the substrate reach the maximum spreading distance. The conservative energy $E_c = E_s + E_k$ exhibits an exponential decay over time

where $\hat{\Omega}$ is fluid volume, \hat{A}_{LV} is liquid-air interface area, and \hat{A}_{SL} is solid-liquid interface area. We used $\hat{\rho}_l \hat{U}_0^2 D_0^3$ to obtain dimensionless form of energies. In Fig. 6, we plot the evolution of the energy (where E_g is gravitational energy and negligible, E_c is the conservative energy and is thus defined with $E_c = E_k + E_s$) over time for $We = 130$, $Re = 1189$. It shows that kinetic energy is partly converted to surface tension energy, which reaches a peak at $\tau \simeq 2.5$, but the kinetic energy is otherwise dissipated directly. The highest dissipation rates are achieved early in the entire process, having reached close to zero by the time of the maximum in surface energy.

For single drop impacts, the viscous dissipation is always difficult to incorporate into a theoretical model [35, 36], and there are similar challenges in pair-drop impacts. However, we see here that for pair-drop impacts, E_c follows an exponential decay, which for the case $We = 130$, $Re = 1189$ presented in Fig. 6, is found through fitting to be $\Delta E_c = 0.7771e^{-1.1876t} + 0.2345$. Thus we estimate the dissipated energy instead by the deviation of the conservative energy from its initial value, yielding $\Delta E_d = -\Delta E_c$. This estimate is preferable to the direct evaluation (11)-(12) because it is simplest to establish convergence with respect to numerical resolution, for the resolutions presented here - see the Supplementary Information. We also the important times t_{imp} , t_{Hs} , and the moment at which the maximum spreading radius is reached on the substrate, $t_{\beta_{max}}$. There is no energy discontinuity at t_{imp} , but E_s noticeably increases after t_{imp} , and reaches its maximum at around $t_{\beta_{max}}$. E_k reaches its minimum at a short time after $t_{\beta_{max}}$, suggesting that some kinetic energy is left in the drops at t_{Hs} . However, the minimum is quite broad and there is little variation in E_k after t_{Hs} . Thus for the purposes of constructing a predictive energetic model, we will in the following approximate $t_{Hs} \simeq t_{\beta_{max}}$ and that E_k reaches its minimum at t_{Hs} .

4.1. Cylindrical disk and lollipop model for the central sheet

In this section, we advance an energetic theory to predict the height of the central sheet at $\hat{t}_{Hs} = t_{Hs} \hat{D}_0 / \hat{U}_0$. In the following we will use dimensionless (uncareted) variables. A schematic of the energetic model is shown in Fig. 7. We model the drops on the substrate with a thin

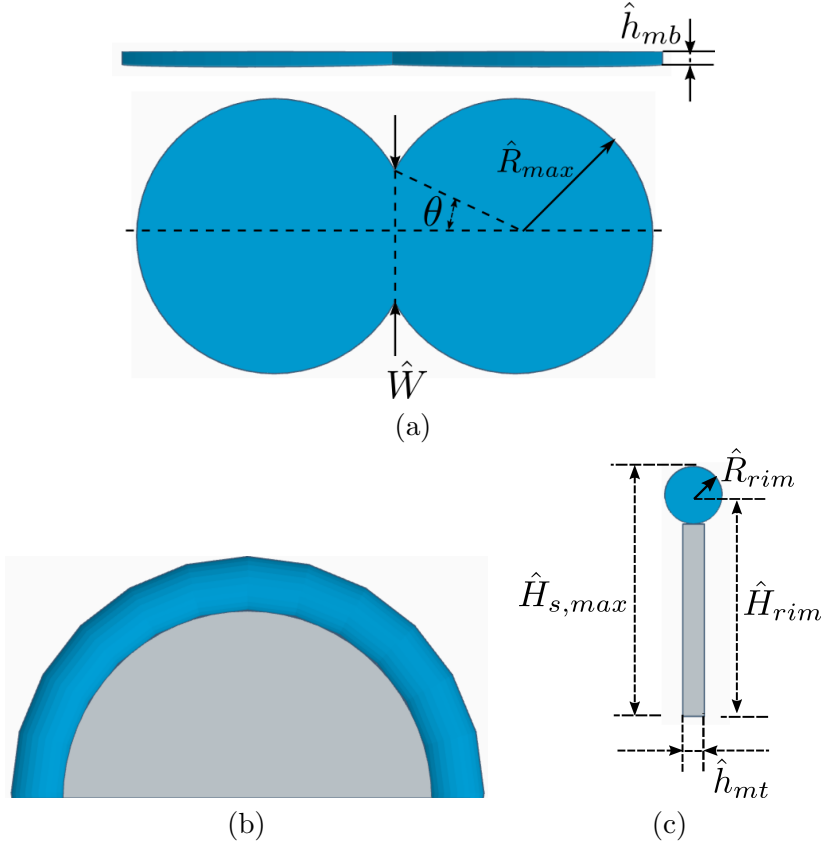


Figure 7: Schematics of the energetic model prediction, illustrating two geometric assumptions: the cylindrical disk and the lollipop models, with the lollipop model shown. For the cylindrical disk assumption, \hat{R}_{rim} is zero

cylindrical disk in Fig. 7(a), with the maximum spreading radius \hat{R}_{max} , uniform thickness \hat{h}_{mb} , half central angle θ , and width \hat{W} for the central sheet. While [18] model the central sheet as a circular segment, we model the lamella itself as an half-ellipse, bordered by a rim with a circular cross-section. In this way, the transverse cross-section in the $x - z$ plane resembles a lollipop.

With this geometry, the variables relevant to the central sheet are the maximum height $\hat{H}_{s,max}$, the elevation of the rim at the lamella periphery \hat{H}_{rim} , the radius of the rim \hat{R}_{rim} , and the thickness of the central lamella \hat{h}_{mt} . When the rim dominates the central sheet dynamics, the lamellar part is thin and thus we assume $\hat{h}_{mt} \simeq 0$; whereas if $\hat{R}_{rim} \simeq 0$, then $\hat{H}_{s,max} = \hat{H}_{rim}$, and $\hat{h}_{mt} \neq 0$, the model resembles a elliptical disk. We consider both of these cases in the following.

Based on the observation from Fig. 6 that there is little variation among all the energetic contributions between \hat{t}_{H_s} and $\hat{t}_{\beta_{max}}$, we assume the central sheet reaches its maximum height at the same time that the drops on the substrate reach their maximum spreading radii, i.e. $\hat{t}_{H_s} \approx \hat{t}_{\beta_{max}}$. We also approximate the remaining kinetic energy in the system to be zero at this time, and use the same equilibrium contact angle $\theta_{eq} = 90^\circ$ as in the simulations. Given the morphology assumptions in Fig. 7, the properties of volume conservation, energy conservation, and geometric confinement can be expressed as [35, 36]:

$$\hat{E}_{s0} + \hat{E}_{k0} = \hat{E}_s + \hat{E}_d \quad (13)$$

$$2\hat{V}_{drop} = \hat{V}_{rs} + \hat{V}_{cs} \quad (14)$$

$$\left(\frac{\hat{W}}{2}\right)^2 + \left(\frac{\Delta\hat{x}}{2}\right)^2 = \hat{R}_{max}^2 \quad (15)$$

Where \hat{E}_{k0} and \hat{E}_{s0} are the initial kinetic energy and surface tension energy respectively, \hat{V}_{drop} is the initial volume of a (single) drop, \hat{V}_{rs} is the volume of the drop remaining on the substrate (i.e. excluding the central sheet), \hat{V}_{cs} is the drop volume of the central sheet, and $\hat{H}_{s,max} = \hat{H}_{rim} + \hat{R}_{rim}$. Therefore, in dimensionless form:

$$\begin{aligned} 2 + \frac{1}{6}We = & 2\frac{\pi - \theta}{\pi}\beta_{max}h_{mb} + \beta_{max}^2\left(\frac{\pi - \theta}{2\pi} + \frac{\sin 2\theta}{4\pi}\right) \\ & + \frac{1}{2}\beta_{max}(H_{rim} - R_{rim})\sin\theta \\ & + \pi R_{rim}\left[\left(3H_{rim} + \frac{3}{2}\beta_{max}\sin\theta\right)\right. \\ & \left.- \sqrt{\left(3H_{rim} + \frac{1}{2}\beta_{max}\sin\theta\right)\left(\frac{3}{2}\beta_{max}\sin\theta + H_{rim}\right)}\right] \\ & + \frac{\hat{E}_d}{\pi\sigma D_0^2} \end{aligned} \quad (16)$$

$$\begin{aligned} \frac{1}{3} = & 2h_{mb}\left(\frac{\pi - \theta}{4\pi}\beta_{max}^2 + \frac{1}{8}\beta_{max}^2\sin 2\theta\right) + \frac{1}{4}(H_{rim} - R_{rim})h_{mt}\beta_{max}\sin\theta \\ & + \frac{\pi R_{rim}^2}{2}\left[3\left(H_{rim} + \frac{\beta_{max}\sin\theta}{2}\right)\right. \\ & \left.- \sqrt{\left(3H_{rim} + \frac{\beta_{max}\sin\theta}{2}\right)\left(\frac{3\beta_{max}\sin\theta}{2} + H_{rim}\right)}\right] \end{aligned} \quad (17)$$

$$\theta = \arccos \frac{\Delta x}{\beta_{max}} \quad (18)$$

$$H_{s,max} = H_{rim} + R_{rim} \quad (19)$$

In this system of four nonlinear algebraic equations, there are seven unknown variables: h_{mb} , β_{max} , W , h_{mt} , $H_{s,max}$, H_{rim} , R_{rim} . By using the lollipop or cylindrical disk model this is reduced to six as $h_{mt} \approx 0$ or $R_{rim} \approx 0$ respectively. Next, based on the maximum spreading ratio comparison in Figure S15 and as reported in Goswami and Hardalupas [18], the central rim collision has little effect on the maximum spreading radius on the parts of the substrate away from the central sheet. Therefore, to close the system, we use the theory of single drop impacts on the substrate for h_{mb} , β_{max} . In Wildeman et al. [36], $h_{mb} = 2/(3\beta_{max}^2)$, and β_{max} can be obtained from:

$$\frac{3(1 - \cos\theta)}{We}\beta_{max}^2 + \frac{0.7}{\sqrt{Re}}\beta_{max}\sqrt{\beta_{max} - 1} = \frac{12}{We} + \frac{1}{2} \quad (20)$$

It remains to estimate \hat{E}_d in (16). We calculate the viscous dissipation in eqn. (16) using an exponential model by assuming $\hat{E}_d = (C_0 - C_0 e^{-Bt})\hat{E}_0$, and obtain $C_0 \approx 0.87(\frac{We^{1.2}}{Re})^{0.09}$, $B \approx 1.75(\frac{We^{1.2}}{Re})^{0.3}$ by fitting according to the dissipation data obtained in the numerical results, so that the dissipation term in eqn. (16) becomes $(2 + We/6)(C_0 - C_0 e^{-Bt})$. Finally, for t_{H_s} in the dissipation model, we ch the scaling $t_{H_s} = 0.08(We^{1/2}Re^{1/10}) + t_{imp}$ by fitting (see §4.2 below) and by subtracting the average $\bar{t}_{imp} \approx 0.425$ for all cases. By solving the energetic

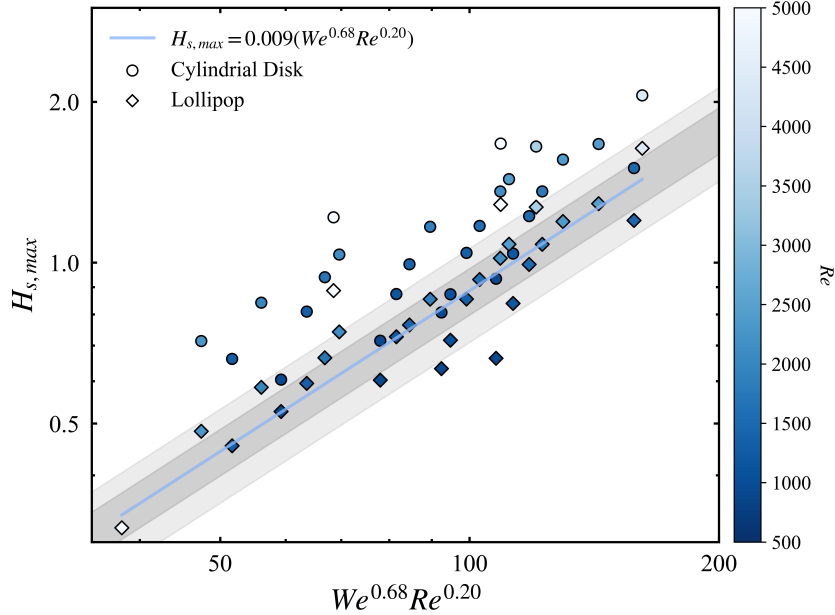


Figure 8: Comparison of the maximum height between the numerical results, shown by the fitted solid line, and the energetic model predictions under the two geometric assumptions

system model in (16)-(20) with the `Sympy` library using the nonlinear equation solver `nsolve` in Python, we can then obtain the height of the central sheet for different cases.

We now test this energetic model against the numerical data. Fig. 8, shows $H_{s,max}$ plotted against a scaling of $We^{0.68}Re^{0.2}$ (see §4.2) on the abscissa, including the numerical results and those from the energetic model in both the lollipop and cylindrical disk expressions. The data are coloured by the value of Re . In comparison with the numerical data, the cylindrical disk model overestimates the height for the most cases, but the lollipop model performs well overall within a 10% error region. For the cylindrical disk model, the model prediction attains 20% error against the numerical result for $Re \gtrsim 1500$, but for $Re \lesssim 1000$ the model nearly overlaps with the numerical results, showing better prediction than the lollipop model. But the lollipop model performs better overall, especially for $1000 \lesssim Re \lesssim 4000$. For $Re \gtrsim 4000$, both models overestimate the maximum height. Overall, the energetic model, especially in the lollipop expression, shows a good ability to predict the height of the central sheet. Discrepancies in the model may be explained by intrinsic errors in the energy model for single drop impacts, nonsimultaneity of t_{H_s} , $t_{\beta_{max}}$ and the kinetic energy minimum, the actual value of the kinetic energy at t_{H_s} , the choice of shape for the central sheet and rim, and the nonuniform thickness of drops on the substrate and of the central sheet.

4.2. Asymptotic height prediction at different Δx

We now consider asymptotic behaviour at large Re and We . First, consider large We in the distinguished limit $Oh \rightarrow 0$ where $Oh = \sqrt{We}/Re$; for comparison, the Oh considered in the numerical simulations does not exceed 0.012. In this limit, surface tension forces dominate, resulting in an asymptotic scaling $\beta_{max} \sim We^{1/2}$ [34, 36] for single drop impacts on the substrate. The leading order result is that, $H_{s,max} \rightarrow \sqrt{We}$ (see below), but this also requires $\beta_{max} \gg \Delta x$, which is not plausible for the problem formulation. This may in principle be corrected by expanding (16)-(20) in an asymptotic series in powers of $We^{-1/2}$, but instead we proceed by simply solving the equations numerically in the limit $Re \rightarrow \infty$, and neglecting \hat{E}_d , for a range

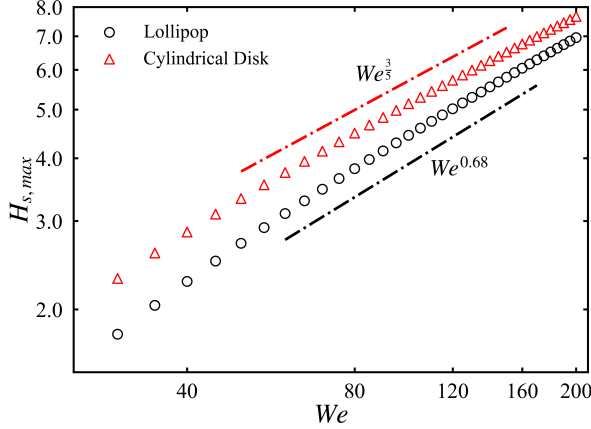


Figure 9: Scaling of $H_{s,\max}$ with We as predicted by the energetic model under the lollipop and cylindrical disk geometric assumptions

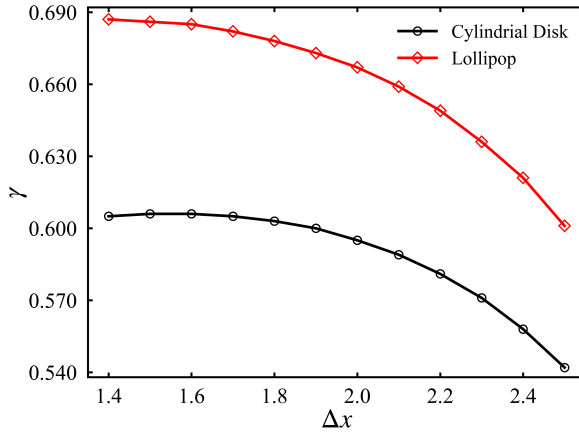


Figure 10: Scaling of $H_{s,\max}$ with We^γ at different Δx as predicted by the energetic model under the lollipop and cylindrical disk geometric assumptions

of values We . For $\Delta x = 1.8$, the results for $H_{s,\max}$ are plotted in Figure 9 for the lollipop and cylindrical disk models respectively. In each case, while the results do not follow a true power law, they can be approximated by one, using an exponent of 0.68, 0.6 respectively.

The closeness of these values to the fractions $2/3, 3/5$ is tantalizing but fortuitous, given that the fitting parameter depends on the range of We being considered, as well as on the value of Δx . Figure 10 shows different approximate scaling laws for $H_{s,\max}$ at different Δx . It shows the exponent of We , namely $H_{s,\max} \sim We^\gamma$, changing with Δx , diamond line points for the lollipop model, and circle line points for the cylindrical disk model. As Goswami and Hardalupas [18] pointed out, the morphology of the central sheet is flat-topped for $\Delta x = 1.3$, so we do not consider smaller inter-drop distance. As Δx increases, γ decreases for both models because more drop bulk is left on the substrate instead of flowing into the central sheet. In addition, the distance has a weaker effect on γ at $\Delta x \lesssim 2$. As Δx increases more, the distance effect plays a more important role on the height, which is more obvious for the cylindrical disk model. We provide further evidence supporting this scaling of $H_{s,\max}$ at different Δx in the supplementary section Appendix B.

Next we seek an heuristic way to estimate the scaling in Re . The above process is difficult to repeat in the distinguished limit $Oh \rightarrow \infty$, namely by taking the limit $We \rightarrow \infty$ and

then solving (16)-(20) numerically for a range of finite Re , because the dissipation term in (16) becomes difficult to handle. In this case, we revert to the leading-order result, namely that the scaling law for $H_{s,max}$ is the same as β_{max} . In the viscous regime $Oh \gg 1$, we have $H_{s,max} \propto \beta_{max} \sim Re^{\frac{1}{5}}$ [34, 36, 38]. The reason for rejecting the leading-order scaling in We in the capillary limit above, but accepting the leading-order scaling for Re in the viscous limit, is that the error incurred by the latter is expected to be somewhat less given that $H_{s,max}$ is less sensitive to Re than We .

The resulting approximate exponents on We (of either 0.68 or 0.6, for $\Delta x = 1.8$) and Re (of 0.2 to leading order, irrespective of Δx) have been obtained in different limits of the parameter Oh and therefore it is not technically appropriate to combine them in a single scaling. We attempt it nevertheless in Fig. 11 where the vertical coordinate is rescaled height ($H_S/(We^{0.68}Re^{0.2})$). The horizontal coordinate has been scaled by $(\tau/(We^{\frac{1}{2}}Re^{\frac{1}{10}}))$, partly informed by the inviscid asymptotic scaling of $t_{\beta_{max}} \sim We^{1/2}$ [42], although the Re-scaling is *ad-hoc*. All the evolution of heights nearly collapse, which suggests that $H_{s,max}$ and t_{H_s} follows these scalings. This is the reason for the abscissa scaling in Fig. 8. Note also that, because $\tau_{cap} \equiv \sqrt{\rho_l D_0^3/\sigma}$, the implication is $t_{H_s} \sim Re^{\frac{1}{10}}\tau_{cap}$.

Finally we remark on the differences in the scaling presented here compared to those of Goswami and Hardalupas [18], Goswami [28]. They show a scaling law on the maximum height given impact Weber number $H_{s,max} \sim 0.16We_{L,imp}^{0.53}$, where $We_{L,imp} \equiv 2\hat{\rho}_l\hat{T}_L\hat{V}_{L,imp}^2/\hat{\sigma}$, and \hat{T}_L and $\hat{V}_{L,imp}$ are the average thickness and velocity of the lamella edges. As we discussed above in §3.1, the dynamics of central rising sheet consists of its lamella and rim dynamics. The thickness of the central lamella is weakly dependent of We and Re , but We dominates the evolution of rims, which means the maximum height is mainly determined by We_{imp} as reported in Goswami and Hardalupas [18], Goswami [28]. The advantage of the present scaling is that it depends directly on the We , Re corresponding to the initial impact, and it is therefore simpler to characterize. Furthermore, the scaling $H_{s,max} \sim We^{0.68}$ obtained from asymptotic behaviour collapses very well the numerical results, capturing the effect of a near-complete conversion of initial kinetic to surface energy, with dissipation playing a secondary role. The role of Re comes in through boundary effects; the exponents on Re in the above scalings appear to work well in explaining the data, but given that this scaling is not technically compatible with that of We , we do not yet have a complete model to explain these, and there may be other choices that also work well.

5. Conclusion

We present high-resolution three-dimensional simulations on the simultaneous pair-drop impacts by solving two-phase Navier-Stokes equations using the *Basilisk* numerical library. A large range of We and Re parameter space is considered in the paper, $15 \leq We \leq 200$ and $938 \leq We \leq 8000$. We mainly investigate the dynamics and energetics of the central sheet, and, in formulating the numerical model, we assumed the dynamics contact angle in the experiment to be approximated by a static contact angle in the numerical simulations. Despite this assumption the simulations were shown to agree well with experiment [18, 28], aside from minor discrepancies. The excellent comparison with experiment highlights the utility of the numerical approach for this problem, and opens up possibilities for many different kinds of multiple-drop impact problems.

A novel energetic model based on simplified "cylindrical disk" and "lollipop" morphologies is proposed, which well predicts $H_{s,max}$ within the parameters in the paper, with marginal

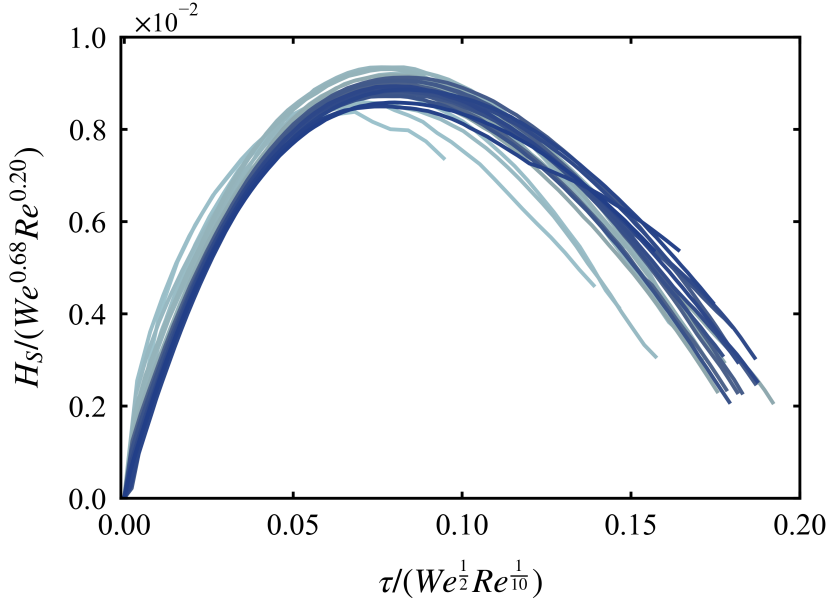


Figure 11: Collapse of the central rising sheet evolution using the scaling law derived from the energetic model in terms of We and Re . The time is collapsed using the capillary time scale ($We^{1/2}$) with a Re correction

error. The viscous dissipation follows an exponential decay that can be easily captured by a fit. The cylindrical disk model overestimates $H_{s,max}$ mostly, especially for $Re \gtrsim 1500$ where the model prediction attains 20% error against the numerical results, but works well for $Re \lesssim 1000$. The lollipop model performs better overall with most of the results falling within 10% error against the numerical results, but shows an overestimation for $Re \gtrsim 4000$. Furthermore, numerically estimated asymptotic solutions are considered under both morphological models. We find approximate scalings of $H_{s,max} \propto We^{0.6}$ for the cylindrical disk model and $H_s \propto We^{0.68}$ for the lollipop model, wherein all the initial energy converts to surface energy at t_{H_s} . The scaling of We for $H_{s,max}$ is weakly dependent on the drop spacing for $\Delta x \lesssim 2$, but decreases beyond this inter-drop distance. Similarly a scaling proportional to $Re^{0.2}$ is suggested in a different limit of the equations. Following these results, an heuristic scaling law $H_{s,max} \sim We^{0.68}Re^{0.2}$ is proposed in terms of the scaling laws obtained from the energetic model. A complete explanation of the Re -scaling is left for future work.

This work contributes to the mechanisms underlying not only pair-drop impacts but also multiple-drop impacts, and further fragmentation investigation of the central sheet. It also opens up many possibilities for other problems including impacts on the thin films or deep pools, and takes the necessary fundamental steps to consider the effects of viscoelasticity or surfactant effects in such impacts.

Acknowledgements

Z. Zhang acknowledges financial support of the Clarendon Fund Scholarships and Magdalen Graduate Scholarships at the Magdalen College of the University of Oxford. Use of the University of Oxford Advanced Research Computing (ARC) facility is also acknowledged. WM and AAC-P acknowledge the Natural Environment Research Council grant UKRI1271. Moreover, AAC-P acknowledges funds from the UK Engineering and Physical Sciences Research Council via grant no. EP/W016036/1).

Declaration of interests

The authors report no conflict of interest.

Author ORCIDs

Z. Zhang <https://orcid.org/0000-0003-3795-7044>; A.A. CAstrejón-Pita <https://orcid.org/0000-0003-4995-2582>; W. Mostert <https://orcid.org/0000-0001-6251-4136>

References

- [1] Y. S. Joung, C. R. Buie, Aerosol generation by raindrop impact on soil, *Nature communications* 6 (2015) 6083.
- [2] A. L. Yarin, Drop impact dynamics: splashing, spreading, receding, bouncing..., *Annu. Rev. Fluid Mech.* 38 (2006) 159–192.
- [3] C. Josserand, S. T. Thoroddsen, Drop impact on a solid surface, *Annual review of fluid mechanics* 48 (2016) 365–391.
- [4] N. Li, Q. Zhou, X. Chen, T. Xu, S. Hui, D. Zhang, Liquid drop impact on solid surface with application to water drop erosion on turbine blades, part i: Nonlinear wave model and solution of one-dimensional impact, *International Journal of Mechanical Sciences* 50 (2008) 1526–1542.
- [5] L. Hulse-Smith, N. Z. Mehdizadeh, S. Chandra, Deducing drop size and impact velocity from circular bloodstains, *Journal of Forensic Sciences* 50 (2005) JFS2003224–10.
- [6] S. Fest-Santini, J. Steigerwald, M. Santini, G. E. Cossali, B. Weigand, Multiple drops impact onto a liquid film: Direct numerical simulation and experimental validation, *Computers & Fluids* 214 (2021) 104761.
- [7] G. Guggilla, R. Narayanaswamy, A. Pattamatta, An experimental investigation into the spread and heat transfer dynamics of a train of two concentric impinging droplets over a heated surface, *Experimental Thermal and Fluid Science* 110 (2020) 109916.
- [8] C.-K. Chen, S.-Q. Chen, W.-M. Yan, W.-K. Li, T.-H. Lin, Experimental study on two water drops successively impinging on a solid surface, *AIP Advances* 10 (2020).
- [9] T. Wibowo, A. Widyatama, S. Kamal, et al., The effect of ethylene glycol concentration on the interfacial dynamics of the successive droplets impacting onto a horizontal hot solid surface, *International Journal of Thermal Sciences* 159 (2021) 106594.
- [10] J. Luo, S.-Y. Wu, L. Xiao, Z.-L. Chen, Hydrodynamics and heat transfer of multiple droplets successively impacting on cylindrical surface, *International Journal of Heat and Mass Transfer* 180 (2021) 121749.
- [11] D. G. Aarts, H. N. Lekkerkerker, H. Guo, G. H. Wegdam, D. Bonn, Hydrodynamics of droplet coalescence, *Physical review letters* 95 (2005) 164503.
- [12] J. Castrejón-Pita, K. Kubiak, A. Castrejón-Pita, M. Wilson, I. Hutchings, Mixing and internal dynamics of droplets impacting and coalescing on a solid surface, *Physical Review E—Statistical, Nonlinear, and Soft Matter Physics* 88 (2013) 023023.

- [13] H. Barnes, Y. Hardalupas, A. Taylor, J. Wilkins, et al., An investigation of the interaction between two adjacent impinging droplets, in: Proceedings of the 15th International Conference on Liquid Atomisation and Spray Systems (ILASS), Toulouse, 1999, pp. 1–7.
- [14] I. V. Roisman, B. Prunet-Foch, C. Tropea, M. Vignes-Adler, Multiple drop impact onto a dry solid substrate, *Journal of colloid and interface science* 256 (2002) 396–410.
- [15] G. Liang, H. Yu, L. Chen, S. Shen, Interfacial phenomena in impact of droplet array on solid wall, *Acta Mechanica* 231 (2020) 305–319.
- [16] A. Gultekin, N. Erkan, E. Ozdemir, U. Colak, S. Suzuki, Simultaneous multiple droplet impact and their interactions on a heated surface, *Experimental Thermal and Fluid Science* 120 (2021) 110255.
- [17] N. E. Ersoy, M. Eslamian, Central uprising sheet in simultaneous and near-simultaneous impact of two high kinetic energy droplets onto dry surface and thin liquid film, *Physics of Fluids* 32 (2020).
- [18] A. Goswami, Y. Hardalupas, Simultaneous impact of droplet pairs on solid surfaces, *Journal of Fluid Mechanics* 961 (2023) A17.
- [19] K. A. Raman, Dynamics of simultaneously impinging drops on a dry surface: Role of inhomogeneous wettability and impact shape, *Journal of colloid and interface science* 516 (2018) 232–247.
- [20] M. Sohag, W. Zhang, X. Yang, Three-dimensional numerical study of two drops impacting on a heated solid surface by smoothed particle hydrodynamics, *Physics of Fluids* 35 (2023).
- [21] V. Sanjay, S. Lakshman, P. Chantelot, J. H. Snoeijer, D. Lohse, Drop impact on viscous liquid films, *Journal of Fluid Mechanics* 958 (2023) A25.
- [22] V. Sanjay, P. Chantelot, D. Lohse, When does an impacting drop stop bouncing?, *Journal of Fluid Mechanics* 958 (2023) A26.
- [23] A. Riviere, W. Mostert, S. Perrard, L. Deike, Sub-hinze scale bubble production in turbulent bubble break-up, *Journal of Fluid Mechanics* 917 (2021) A40.
- [24] W. Mostert, S. Popinet, L. Deike, High-resolution direct simulation of deep water breaking waves: transition to turbulence, bubbles and droplets production, *Journal of Fluid Mechanics* 942 (2022) A27.
- [25] K. Tang, T. Adcock, W. Mostert, Bag film breakup of droplets in uniform airflows, *Journal of Fluid Mechanics* 970 (2023) A9.
- [26] H. Wang, S. Liu, A.-C. Bayeul-Lainé, D. Murphy, J. Katz, O. Coutier-Delgosha, Analysis of high-speed drop impact onto deep liquid pool, *Journal of Fluid Mechanics* 972 (2023) A31.
- [27] S. Popinet, Numerical models of surface tension, *Annual Review of Fluid Mechanics* 50 (2018) 49–75.
- [28] A. Goswami, Impact of Multiple Droplets on Solid Surfaces, Phd thesis, Imperial College London, 2023.

- [29] S. Popinet, Basilisk flow solver and pde library, available at available at <http://basilisk.fr> (2020).
- [30] S. Popinet, An accurate adaptive solver for surface-tension-driven interfacial flows, *Journal of Computational Physics* 228 (2009) 5838–5866.
- [31] J. B. Bell, P. Colella, H. M. Glaz, A second-order projection method for the incompressible navier-stokes equations, *Journal of computational physics* 85 (1989) 257–283.
- [32] J. U. Brackbill, D. B. Kothe, C. Zemach, A continuum method for modeling surface tension, *Journal of computational physics* 100 (1992) 335–354.
- [33] I. V. Roisman, Inertia dominated drop collisions. ii. an analytical solution of the navier–stokes equations for a spreading viscous film, *Physics of Fluids* 21 (2009).
- [34] J. Eggers, M. A. Fontelos, C. Josserand, S. Zaleski, Drop dynamics after impact on a solid wall: theory and simulations, *Physics of fluids* 22 (2010).
- [35] C. Ukiwe, D. Y. Kwok, On the maximum spreading diameter of impacting droplets on well-prepared solid surfaces, *Langmuir* 21 (2005) 666–673.
- [36] S. Wildeman, C. W. Visser, C. Sun, D. Lohse, On the spreading of impacting drops, *Journal of fluid mechanics* 805 (2016) 636–655.
- [37] N. Laan, K. G. de Bruin, D. Bartolo, C. Josserand, D. Bonn, Maximum diameter of impacting liquid droplets, *Physical Review Applied* 2 (2014) 044018.
- [38] J. M. Gordillo, G. Riboux, E. S. Quintero, A theory on the spreading of impacting droplets, *Journal of Fluid Mechanics* 866 (2019) 298–315.
- [39] J. Du, X. Wang, Y. Li, Q. Min, X. Wu, Analytical consideration for the maximum spreading factor of liquid droplet impact on a smooth solid surface, *Langmuir* 37 (2021) 7582–7590.
- [40] P. Attané, F. Girard, V. Morin, An energy balance approach of the dynamics of drop impact on a solid surface, *Physics of Fluids* 19 (2007).
- [41] S. Ray, Y. Han, Z. Yue, H. Guo, C. Y. H. Chao, S. Cheng, New insights into head-on bouncing of unequal-size droplets on a wetting surface, *Journal of Fluid Mechanics* 983 (2024) A25.
- [42] A. Amirfazli, M. D. Bustamante, Y. Hu, L. Ó Náraigh, Bounds on the spreading radius in droplet impact: the inviscid case, *Proceedings of the Royal Society A* 480 (2024) 20230760.
- [43] S. Batzdorf, J. Breitenbach, C. Schlawitschek, I. V. Roisman, C. Tropea, P. Stephan, T. Gambaryan-Roisman, Heat transfer during simultaneous impact of two drops onto a hot solid substrate, *International Journal of Heat and Mass Transfer* 113 (2017) 898–907.
- [44] B. Zhang, V. Sanjay, S. Shi, Y. Zhao, C. Lv, X.-Q. Feng, D. Lohse, Impact forces of water drops falling on superhydrophobic surfaces, *Physical review letters* 129 (2022) 104501.
- [45] Y. Wang, L. Bourouiba, Drop impact on small surfaces: thickness and velocity profiles of the expanding sheet in the air, *Journal of Fluid Mechanics* 814 (2017) 510–534.

- [46] K. Tang, T. Adcock, W. Mostert, Fragmentation of colliding liquid rims, *Journal of Fluid Mechanics* 987 (2024) A18.
- [47] A. L. Yarin, D. A. Weiss, Impact of drops on solid surfaces: self-similar capillary waves, and splashing as a new type of kinematic discontinuity, *Journal of fluid mechanics* 283 (1995) 141–173.

Numerical simulations of simultaneous pair-drop impacts and their energetics
 The central rising sheet of simultaneous pair-drop impacts:
 Supplementary Material

Ziyao Zhang^{b,*}, Alfonso A. Castrejón-Pita^b, Wouter Mostert^b

^b*Department of Engineering Science, University of Oxford, Oxford, OX1 3PJ, United Kingdom*

Appendix A. Numerical verification and validation

Here, we present extra information about verification and validation for the simulations. In the experiments [18, 28], a smooth acrylic substrate with advancing angle $80 \pm 2^\circ$ and receding angle $58 \pm 2^\circ$. For the numerical problem, superhydrophobic or fully wetting boundary conditions for the volume fraction f are not suitable. For superhydrophobic substrates, splashing behavior appears easily but requires a relatively fine grid to resolve satisfactorily. On the other hand, when fully wetting boundary conditions are considered, it is thin film impact [2]. Therefore, in the numerical simulations a static contact angle $\theta_s = 90^\circ$ is used on the impact substrate as an approximation. As shown in Fig. S1, the whole simulation domain is presented and the grid is refined around two drops at initialization.

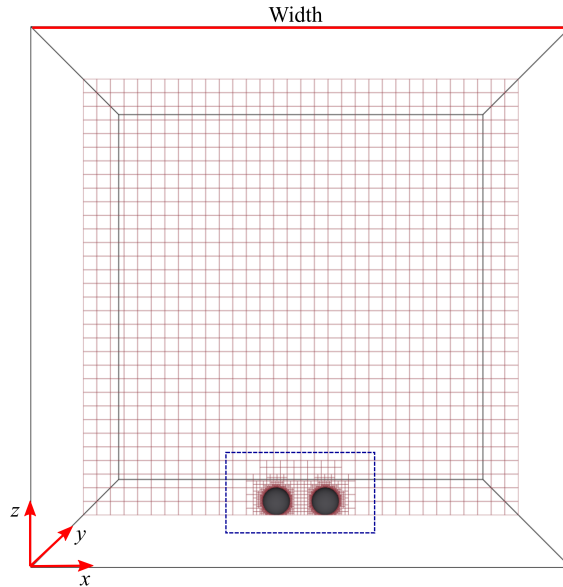


Figure S1: Computational domain illustrating the adaptive grid refinement around the two drops

Appendix A.1. Mesh convergence study

Mesh convergence test is shown in this section. In Figure S2 the nondimensional heights of rising sheet ($H_s = \hat{H}_s / \hat{D}_0$, we omit the star for clarity in the following) at central of two

*Corresponding author

Email address: ziyao.zhang@eng.ox.ac.uk (Ziyao Zhang)

drops for $\phi = 0\%$, $We = 54$, $Re = 3581$, $\rho_r = 813$, $\mu_r = 56$ and $\phi = 40\%$, $We = 130$, $Re = 1189$, $\rho_r = 910$, $\mu_r = 269$ evolving with nondimensional time ($\tau = tU_0/D_0$) are compared with experimental data. The large density ratio leads to a stiff coefficient matrix and causes numerical problems in two-phase flow, which is a general problem for the simulations of 40% glycerol-water solutions. Therefore, to ensure stability, the Poisson solver within the numerical code run for a fixed number of iterations N . We verify first that the numerical results are insensitive to the choice of N , and that they compare well with experiment.

For the case of distilled water drops, we compare numerical results obtained with or without the minimum iteration method with experimental results. In Figure S2(a), the evolution of H_s is shown versus τ . The points are experimental results in Goswami and Hardalupas [18], Goswami [28], and the lines represent numerical data with different choices of N . In terms of $\phi = 0\%$, namely water drops, three different minimum iteration numbers $N = 5, 10, 20$ are taken into consideration and presented as dotted lines, obtained with a default Poisson solver, which is considered the reference numerical case. It is shown that the data is insensitive to the choice of N . The relative errors for maximum height are 3.56%, 2.88%, 0.38% for $N = 5, 10, 20$ respectively concerning the reference numerical case. Moreover, they all collapse very well with experiment results. For $\phi = 40\%$, hollow points are experimental results in Goswami [28], and dashed point lines are numerical results. The numerical and experimental results collapse extremely well, and relative errors at maximum height are 1.45% and 0.43% as N increase from 5 to 10 and from 10 to 20 respectively. Therefore, $N = 20$ can solve well the parameter space considered in this paper.

The numerical results in Figure S2(a) are obtained through a symmetric configuration, in which means one drop is initialized at the beginning and a symmetric boundary condition is set at the middle interaction surface of two drops [43]. This is illustrated and compared in detail in the following. We next determine the effect of the symmetry plane, compared with the approach where both drops are resolved within the domain. For this study, the grid convergence test is carried out using drops of a 40% glycerol-water solution with the same parameters as used by Goswami [28] at $We = 130$. As presented in Figure S2(b), it indicates that results obtained from symmetric and pair impact configuration are fairly close and agree well with experimental results with $\phi = 0\%$. The size of the computational domain for symmetric configuration is half that of the pair impact configuration, namely $8D_0$. Therefore, the maximum grid resolution is the same for $L_{sym} = 10$ and $L_{pr} = 11$, and $L_{sym} = 11$ and $L_{pr} = 12$, and thus the relative errors at the maximum height between symmetric and drop pair configuration at two resolutions are 4.94% and 6.07% respectively. Hence, the drop pair configuration is chosen for most numerical cases as it gives the better agreement with experiment.

In order to study the grid convergence of the energetics of the process, we plot the volume-integrated energy normalized by its initial value, comprising the initial kinetic (KE) and surface tension (SE) energies, in Fig. S3 for $We = 130$, $Re = 1189$. We include different maximum grid levels to inspect sensitivity to mesh resolution. The energetics of the conservative quantities (namely KE, SE) are individually grid-converged, as is their sum.

Furthermore, a grid resolution study is carried out through pair configuration at $\phi = 40\%$, $We = 130$, compared with experimental results as presented in Figure S2(b). As L increases, the errors at t_{H_s} are 2.92% and 1.11% respectively, which means the results are grid converged. Moreover, we compared the normal force on the substrate for the same parameters

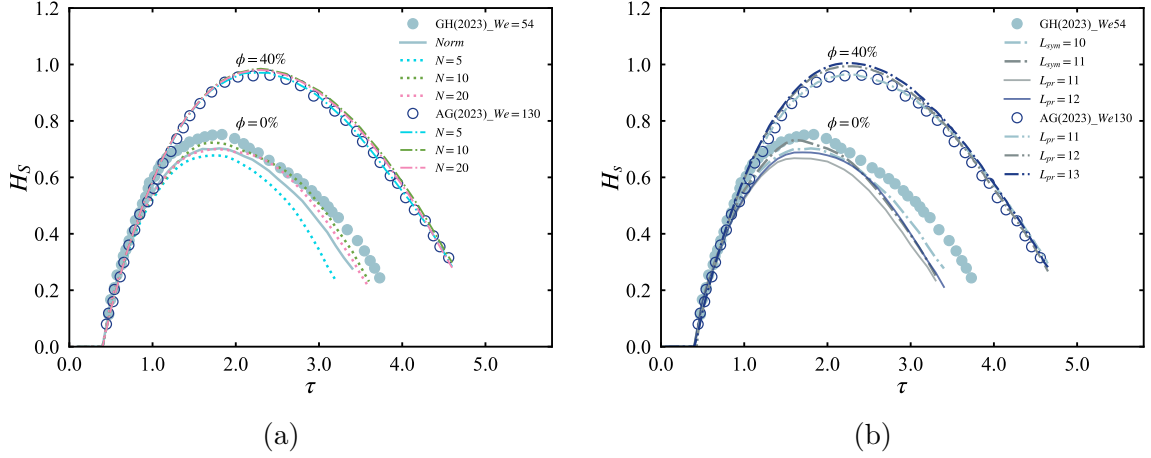


Figure S2: Verification of the numerical method through comparisons of the central rising sheet height: (a) comparison with experiments for different iteration numbers N , and (b) comparison between two numerical configurations and maximum resolution levels for two representative cases, namely $\phi = 0\%$, $We = 54$, $Re = 3581$ and $\phi = 40\%$, $We = 130$, $Re = 1189$. Here, $H_s = \hat{H}_s / \hat{D}_0$ and $\tau = \hat{t} \hat{U}_0 / \hat{D}_0$. Note: the experimental data are adapted from Goswami and Hardalupas [18], Goswami [28]

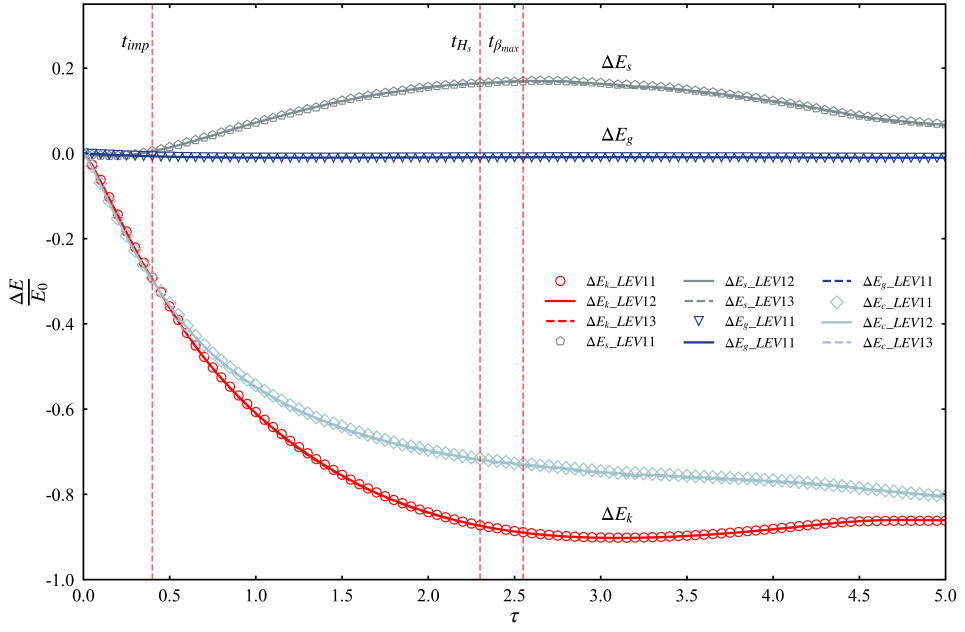


Figure S3: Evolution of the normalized energy variations for different maximum grid resolutions at $We = 130$ and $Re = 1189$. Here, t_{imp} denotes the impact time, t_{H_s} the time of maximum sheet height, and $t_{\beta_{max}}$ the time at which the remaining drops on the substrate reach the maximum spreading distance. The change in conservative energy ΔE_c , exhibits an exponential decay over time. ΔE_s denotes the change in surface energy, ΔE_g the change in gravitational energy, which remains negligible, and ΔE_k the change in kinetic energy

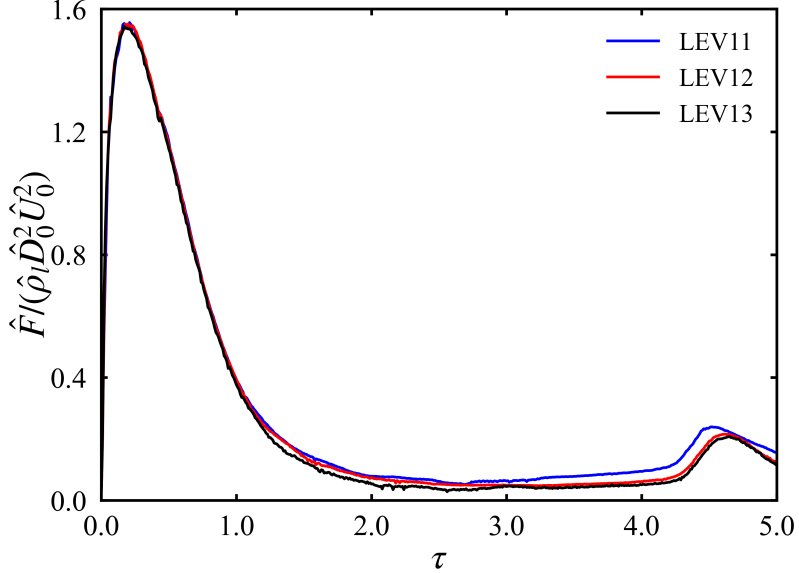


Figure S4: Convergence test of the evolution of the normalized normal force on the substrate for different grid resolution levels at $\phi = 40\%$, $We = 130$, and $Re = 1189$

and it can be expressed as equation A.1 [44]:

$$\hat{F}(\hat{t}) = \left(\int_{\hat{A}} (\hat{p} - \hat{p}_0) d\hat{A} \right) \mathbf{z} \quad (\text{A.1})$$

where \hat{p} is the dynamic pressure on the substrate, \hat{p}_0 is environmental pressure, \hat{A} is substrate's area, and \mathbf{z} is the unit vector normal to the substrate. As shown in Figure S4, the evolution of \hat{F} has two peak values. The first peak is because of the impact of these two drops, and the second peak is due to the impact of the central sheet. The force at early time collapses fairly well with different L . We thus compared the relative errors of the second peak, which are 9.77% and 3.72% respectively. Therefore, we run the simulations with $L = 12$ in this research.

Appendix A.2. Experimental comparison

Since we get converged results using $N = 20$, $L = 12$ in the section above, we compare the results obtained from numerical simulations with experiments [18, 28] by using the settings in the following. Various We are examined with corresponding Re for the distilled water ($\phi = 0\%$) and 40% glycerol-water ($\phi = 40\%$) mixtures.

Fig. S5 presents pair-drop impact at $We = 54$, $Re = 3581$, which corresponds to a distilled-water problem. There is general agreement between numerical and experimental process. First (Fig. S5(a)), the sheet rises due to inertia and then falls because of surface tension [14, 18]. The typical semilunar shape is captured numerically [15, 17, 18], as shown in the side view in Fig. S5(b).

The corresponding quantitative comparison of central sheet height evolution between numerical data and experimental results in Goswami and Hardalupas [18], Goswami [28] is presented in the main text Fig. 4(a) and Fig. 4(b). There are small differences in nominal diameter between Goswami [28] and Goswami and Hardalupas [18]; here we use the former study to determine Reynolds numbers for comparison. As shown in the main text Fig. 4(a), the height evolution matches well with experimental data at three different We . According to Fig. S5, the structure of the central sheet resembles a well-defined semilunar shapes. At larger times, when

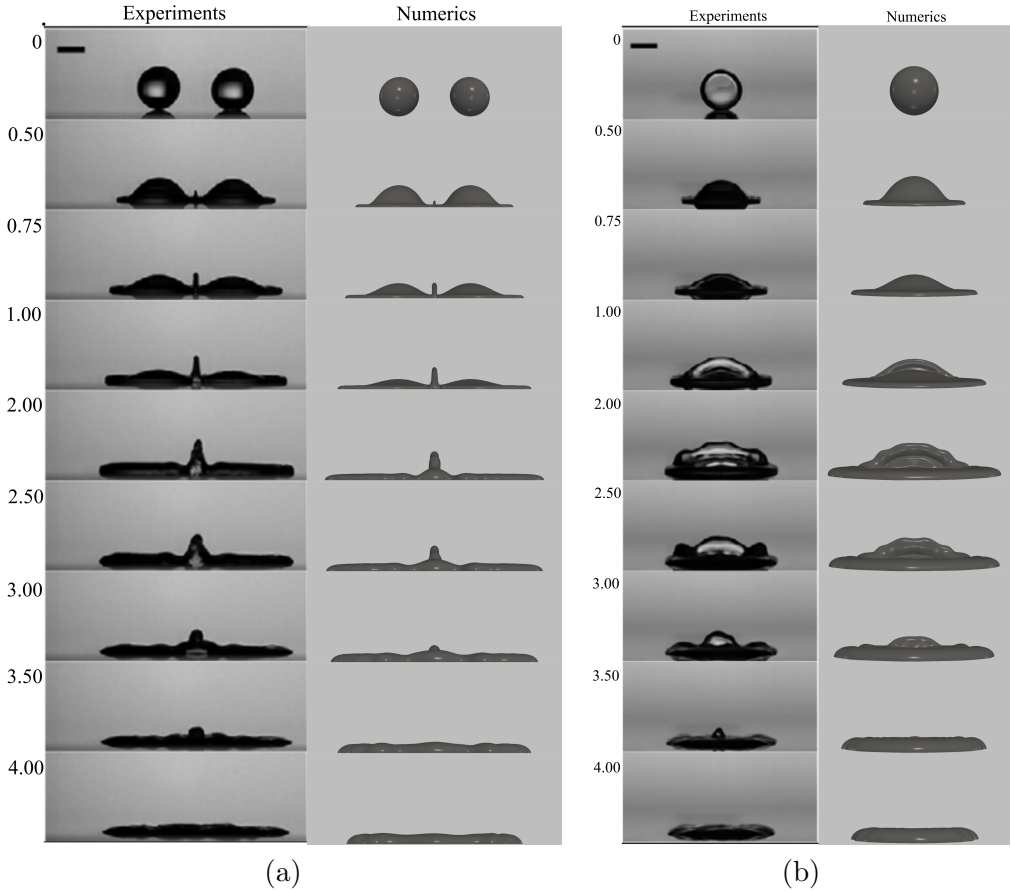


Figure S5: Comparison of the evolution of the central sheet with non-dimensional time between numerical simulations and experiments for distilled water drops at $We = 54$ and $Re = 3581$: (a) front view and (b) side view. Note: the experimental images are adapted from Goswami and Hardalupas [18], CC BY 4.0

the central sheet starts to fall, there is a slight deviation between experimental and numerical curves. To explain this, in Fig. S6, the comparison of volume function f with experiments at different τ with different We is used to illustrate the differences. As shown in Fig. S6(a) and (b), the corrugations develop at the falling stage, and thus induce cusps. These cusps influence the manner in which the maximum height is measured: in the present study we use the geometrical maximum value of the height, which is defined in the main text, while Goswami and Hardalupas [18] determined the maximum height using a fitted circle.

The cusps seen in Fig. S6 are associated with instability of the central sheet. At higher We and Re , some cusps may pinch off, signalling splashing, as shown in Fig. S7. There are specific differences for cusp growth and splashing behaviours between numerical and experimental data. These differences may be attributed to many effects, such as the differences in contact angle, deviation from spherically symmetric drops, or from true simultaneous impact in the experiments, which cannot be quantitatively accounted for in this comparison. Nevertheless the overall agreement between simulation and experiment is excellent. And as we mentioned in the main text, the agreement between experimental and numerical results is further improved for the glycerol-water mixture ($\phi = 40\%$).

All of the validation and verification efforts indicate that our numerical platform captures well the physical process of simultaneous pair-drop impacts. The remainder of the study will describe the results of a comprehensive and cohesive analysis of the dynamics of two simultaneous impact drops across a large regime of parameter space. Since the splashing phenomenon

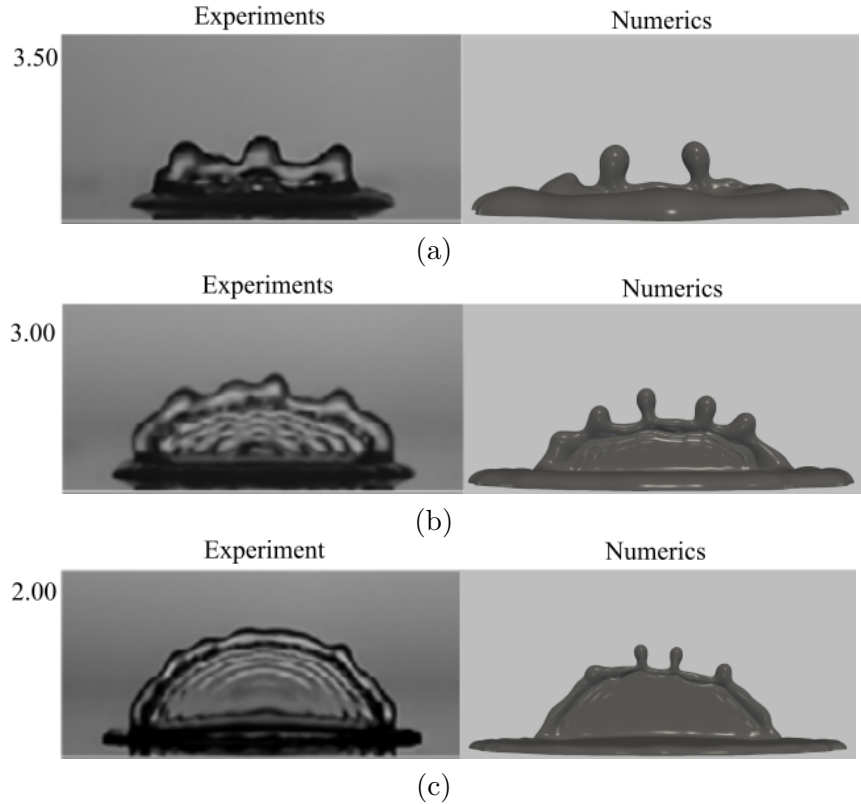


Figure S6: Snapshots of experimental and numerical results at the same non-dimensional time for different We at $\phi = 0\%$: (a) $We = 80$, $Re = 4358$; (b) $We = 104$, $Re = 4969$; and (c) $We = 128$, $Re = 5513$. Note: the experimental snapshots are adapted from Goswami and Hardalupas [18], CC BY 4.0

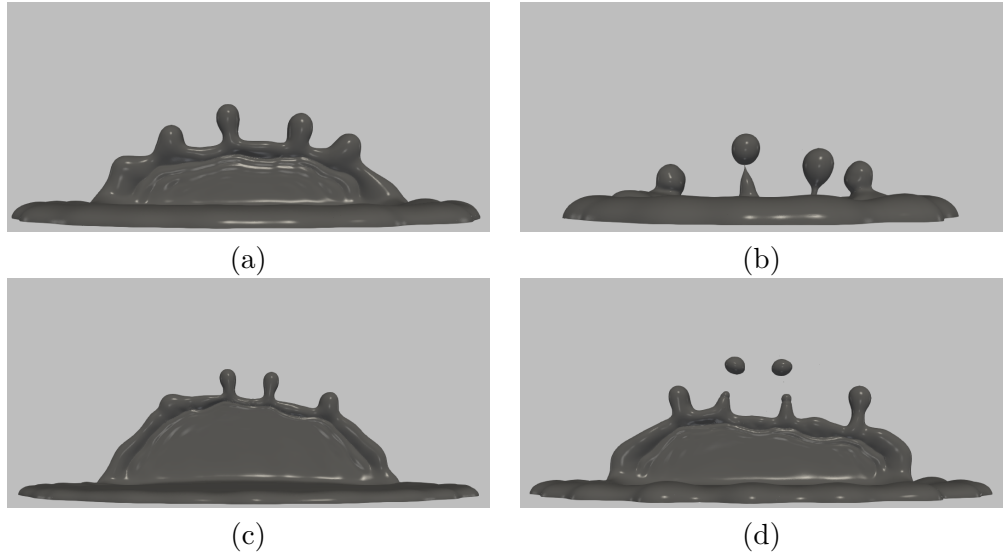


Figure S7: Snapshots of numerical simulation results f for $\phi = 0\%$ at $We = 104$, $Re = 4969$: (a) $\tau = 3$ and (b) $\tau = 4.4$, and at $We = 128$, $Re = 5513$: (c) $\tau = 2$ and (d) $\tau = 3$

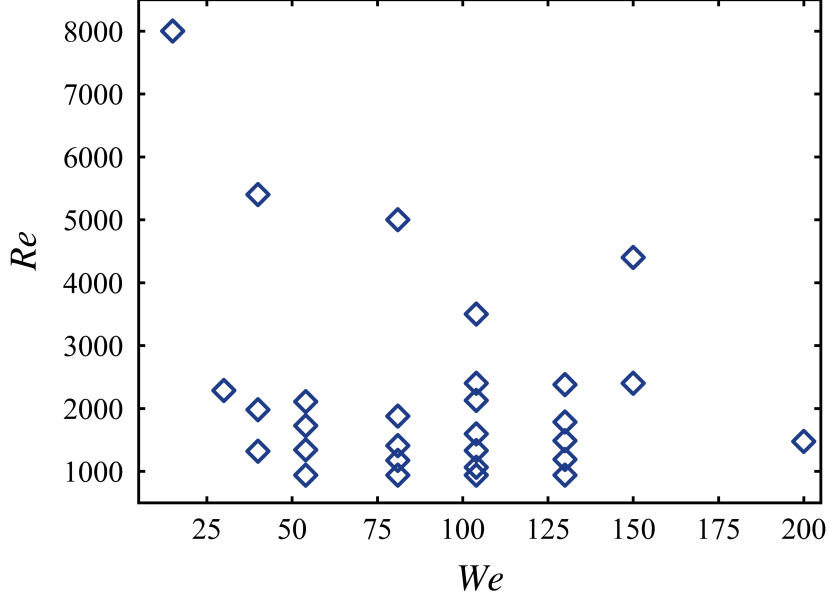


Figure S8: Computational parameter space in terms of We and Re for simultaneous pair-drop impacts

and growth of the central sheet instability are not the principal focus of this paper, in the study we mainly examine impact parameters corresponding to drops of a $\phi = 40\%$ glycerol-water solution. The parameter space as shown in Fig. S8 covers existing experimental parameters in Goswami [28] and extends them. In this work, the cases are set with $L = 12$ in pair impact configuration. For reference, example dimensional properties for $\phi = 40\%$ are: $\rho_l = 1114.5 \text{ kg/m}^3$, $\mu_l = 4.814 \text{ mPa}$, $\sigma = 69.6 \text{ mN/m}$, $D = 3.25 \text{ mm}$.

Appendix B. Scaling comparison at different drop separation distance

We obtain the scalings for $H_{s,max}$ at different Δx through the energetic model in the large Re regime. In this section, we consider the effectiveness of the proposed scalings. We plot the rescaled height evolution with fixed $Re = 938$ for three different $We = 54, 81, 104$ at $\Delta x = 1.5$ in Figure S9(a) and (b), and $We = 81, 104, 130$ at $\Delta x = 2.2$ in Figure S9(c) and (d). H_s is rescaled by the scaling obtained from lollipop model and cylindrical disk model, and τ is rescaled by capillary time $\tau_{cap} \equiv \sqrt{\hat{\rho}_l \hat{D}_0^3 / \hat{\sigma}} = We^{\frac{1}{2}}$. The height profiles are aligned well with the cylindrical disk model $H_{s,max} \sim We^{0.606}$ and lollipop scaling $H_{s,max} \sim We^{0.686}$ at $\Delta x = 1.5$, and the maximum relative error for $H_{s,max}$ at t_{H_s} is 6.25% and 12.8% respectively. At $\Delta x = 2.2$, the maximum relative error for $H_{s,max}$ at t_{H_s} is 12.5% and 15.1% for lollipop model and cylindrical disk model respectively. It indicates that the energetic model works well even considering different Δx , and the cylindrical disk asymptotic scaling works better than lollipop model at smaller drop separation distance, and vice versa. In addition, t_{H_s} is well aligned with τ_{cap} .

Appendix C. Morphology of the central sheet

Appendix C.1. Morphology and height of the central rising sheet

A central sheet rises after two drops interact on the substrate, as reported in Liang et al. [15], Ersoy and Eslamian [17], Goswami and Hardalupas [18] as seen in Fig. S5. This typical semilunar central sheet plays a crucial role in pair-drop impact and even multiple drop impact,

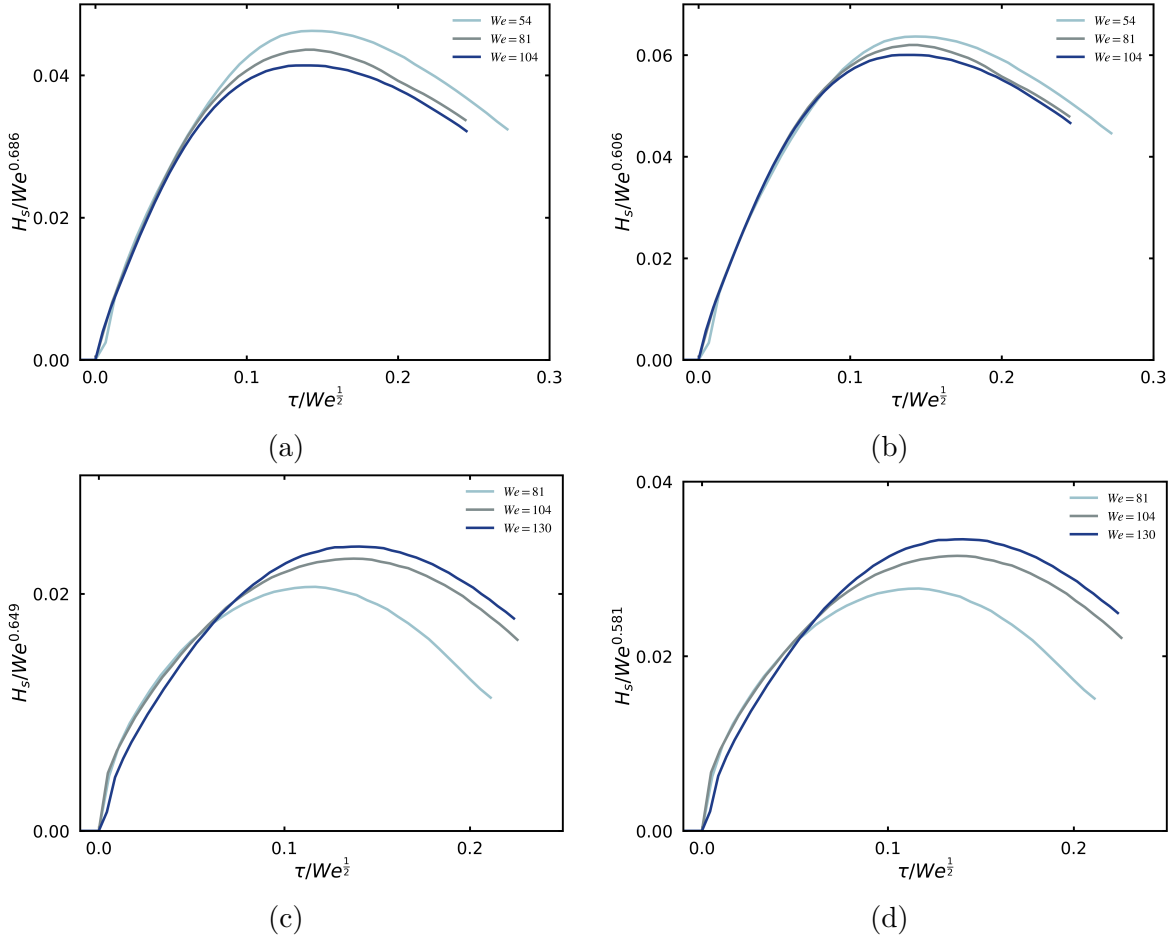


Figure S9: Validation of numerical simulation results collapsed using the scaling law for $H_{s,\max}$ in terms of We , as predicted by (a,c) the lollipop model and (b,d) the cylindrical disk model at $\Delta x = 1.5$ and 2.2, respectively, with fixed $Re = 938$

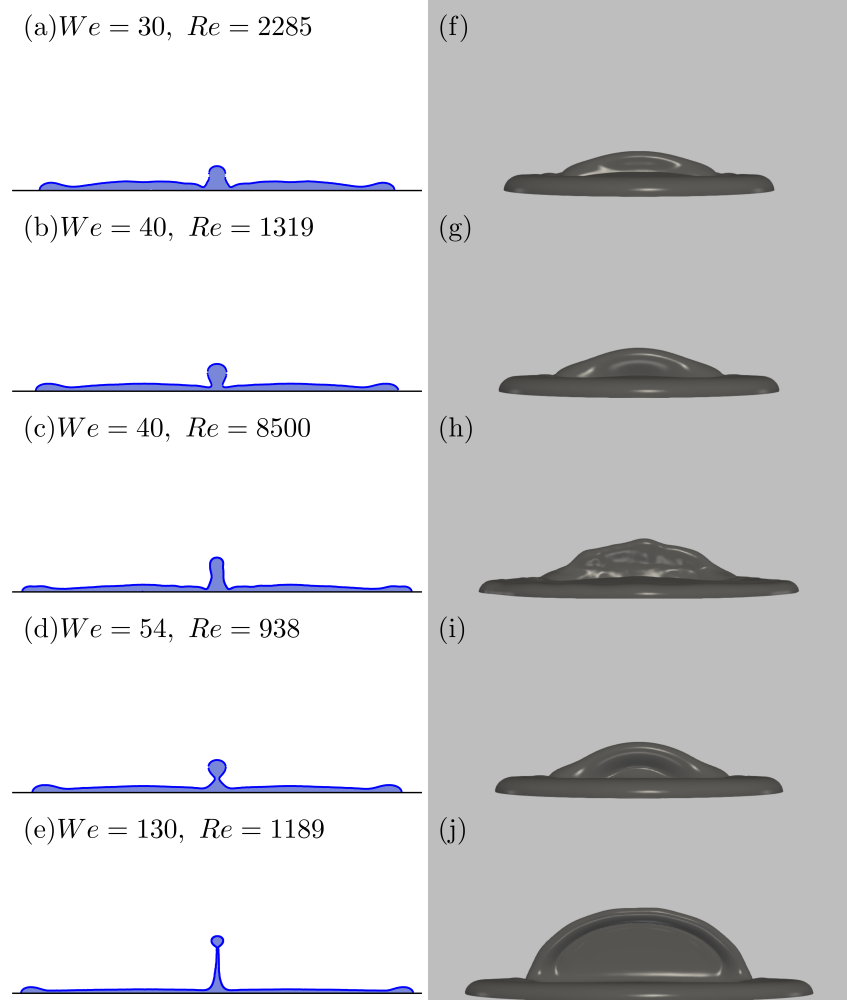


Figure S10: Morphological changes of the central rising sheet with increasing We , shown by front views with two-dimensional slices (left column) and side views represented by the volume fraction f (right column)

and may lead to splashing, where it would otherwise not be expected for single-drop impacts [17, 18]. In this section, a detailed investigation of its morphology will be carried out.

We compare the morphology of the central sheet at the moment it reaches the maximum height. In Fig. S10, different morphologies are shown for different We and Re . The left column is a 2D slice across the centre of the configuration from the front view, and the right column is from the side view. From the front view, the central sheet is low and thick for low We . Even though the sheet becomes thinner with increasing Re as presented by Fig. S10(b) and (c), a more obvious rim on the central sheet appears for $We \geq 54$. As We increases to 130, the central sheet becomes thinner and reaches a higher maximum height. In other words, when $We < 40$, central sheet is thick and low and close to a cylindrical disk. As $We \geq 54$, it tends to resemble a "lollipop". This indicates that We dominates the morphology of central sheet.

Moreover, from the side view, the typical semilunar structure is not present when We is low. For higher Re e.g. Fig. S10(h), rim corrugations appear, owing to a combination of Rayleigh-Taylor and Rayleigh-Plateau instabilities, and dominated by the fastest growing mode Rayleigh-Plateau instability at large time [18]. As We increases, the semilunar structure appears as shown in Fig. S10(j). These observations suggest that We plays a more important role in the morphologies of central sheets than Re , and as We increases the sheet at first features a low and thick cylindrical disk and later on a high and thin lollipop model.

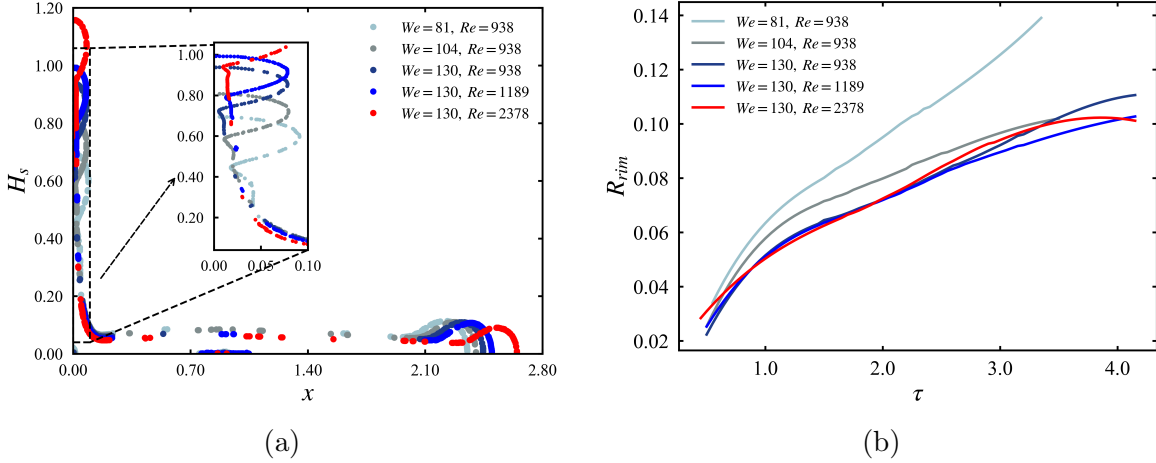


Figure S11: Dimensionless measurements of the central rising sheets: (a) half of the rising sheet including the bottom spreading region, and (b) evolution of the rim radius on the central sheet for different We and Re

We further investigate the thickness of the central sheet at its maximum height and the radius of the central rim in Fig. S11. In Fig. S11(a), we plot the thickness of the central sheet at its maximum height. The central rising sheet consists of a lamella and a rim, similarly to the structure of the spreading drop on the substrate. It shows that the thickness of lamella part varies little with We and Re . Given Fig. S11(b), the evolution of R_{rim} on the central sheet is shown for the same values of We and Re . Generally, R_{rim} increases with time and the time evolution of rims is strongly dependent on We and insensitive to Re . The dynamics of the lamella and the rim on the central sheet is similar to the behaviours of drop spreading on the substrate or that of rim collision [38, 45, 46]. In addition, the rim is only affected by surface tension in early time. Further details on how R_{rim} is measured are given in section §Appendix E.

Finally, Fig. S12 shows the effects of surface tension and viscosity on the height of central rising sheet, through We , Re . In each of Fig. S12(a,b), the evolution of H_s is shown in terms of one varying dimensionless number at a time, where the reference case is $We = 80$, $Re = 938$.

Both We , Re affect the dynamics of the central sheet, though to different extents, as suggested in Fig. S12(a,b). With the increase of We , the maximum heights and the corresponding maximum times $t_{H_s} = t(H_s = H_{s,max})$ increase, because the central sheet rises over a longer time to its maximum value. Similar observations can be made from Fig. S12(c) regarding Re , although here t_{H_s} is approximately invariant; thus clearly in these problems surface tension controls t_{H_s} .

Appendix D. Kinematics of the central sheet

In this section, we turn to the kinematics in the central rising sheet. As given in Fig. S13, we plot vertical velocity (u_y) of the central sheet at t_{H_s} for $We = 130$, $Re = 1189$, $Fr = 78$. u_y is divided into five regions according to the characteristics: in region i (the vortex region) at the base of the rising sheet, there is a vortex and flow recirculates near the substrate. The thickness of this region is around the same order as the thickness of bottom lamella. Region ii, the impact pulse region, shows a rapid gain in velocity which decays over time as shown in Fig. S14(a). Region iii describes the main lamellar part of the rising sheet, and shows a gentler increase in velocity. Region iv, describes the transition from the lamella part to the rim, and shows a rapid increase in velocity because of necking behaviour. Region v describes the rim.

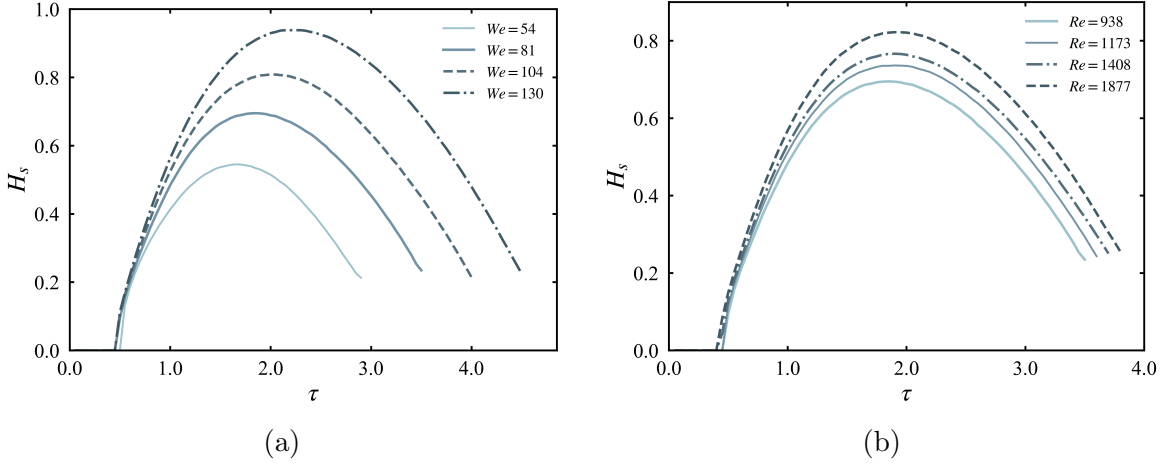


Figure S12: Variations of the central rising sheet height with changes in (a) We and (b) Re . Note: the reference case in each comparison is $We = 80$, $Re = 938$, and only one dimensionless number is varied in each panel

For the same case, we further investigate u_y of the central sheet over time. In Fig. S14(a), we plot u_y at different times from early rising time to t_{H_s} . Generally, u_y decreases with time at fixed y . Regions i and ii almost disappear at large time, such as $\tau = 2.3$. It is well-known that, for single-drop spreading on a substrate, velocity in the lamellar part follows e.g. an r/τ scaling [38, 45–47], but Fig. S14(b) shows that the corresponding scaling of $u_y \approx \frac{y}{\tau - t_{imp}}$ for the present case, where t_{imp} is the rim collision time marking the formation of the central sheet, does not explain the data. This suggests that Regions i and ii, which are missing from the cited cases, plays a strong role in setting the velocity profile in the central sheet. A clear dynamic model accounting for this velocity profile is left for future work.

Furthermore, we compare the maximum spreading factor with previous theories. As shown in Fig. S15, all numerical cases are plotted as black circles, and the hollow points indicate various predictions for β_{max} from the literature for single-drop impact at the given parameters. Different regimes are stand for different We ranging from 15 to 200, and in each regime predicted and measured β_{max} increases with Re . β_{max} is not affected significantly by central interaction, which is also specified in Goswami and Hardalupas [18]. Our numerical data is in general agreement with most models in the literature with respect to both We and Re . Moreover, our data is in closest agreement with Wildeman et al. [36], and this fact is used in the energetic model development.

Appendix E. Data processing details

In this section, we provide a detailed explanation of the method used to plot R_{rim} , which is located at the maximum width of the rim on the central sheet. At early times the rim has not yet formed or its position is obscured by the central sheet, or by the drop bulk on the bottom, but we locate it by searching from the top of the central sheet. If it assumed that the rim grows monotonically (complicated somewhat by the adaptive nature of the grid), we then obtain an approximate location at each time as the original data shown in Fig. S16. Only original data for level 12 are presented, while other results are shown with the smoothed lines for clarity. The error bar for the R_{rim} is 5%. The relative error of the smoothed R_{rim} at t_{H_s} are 5.63% and 1.65% respectively with different levels. We conclude that the data, processed using this method, are grid converged to obtain R_{rim} , and the evolution profiles of R_{rim} shown in the main text are smoothed profiles within a 5% error bar.

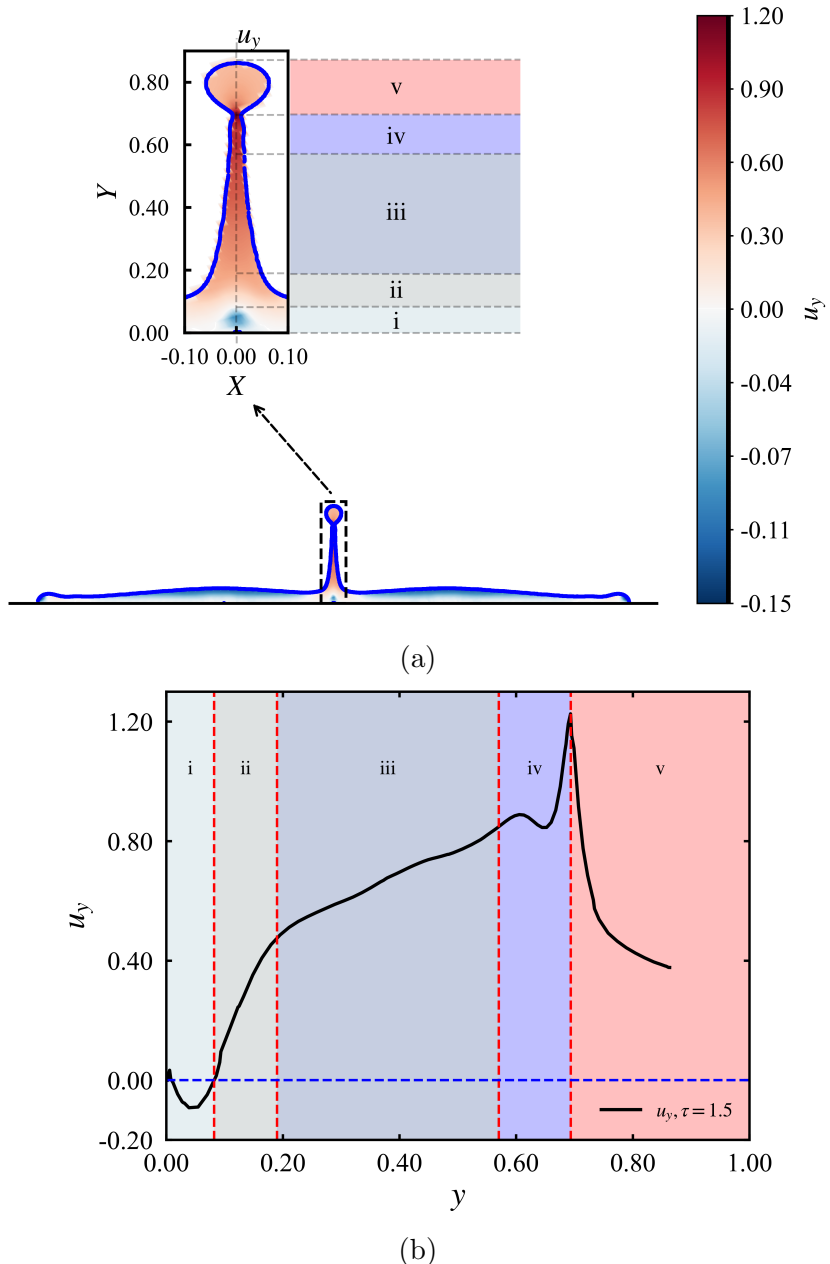


Figure S13: (a) Two-dimensional slice of the vertical velocity field of the central rising sheet: region i the vortex region; region ii the impact pulse region; region iii the main lamellar part of the rising sheet; region iv the transition from the lamella to the rim; and region v the rim. (b) Vertical velocity u_y along the central line at $We = 130$ and $Re = 1189$

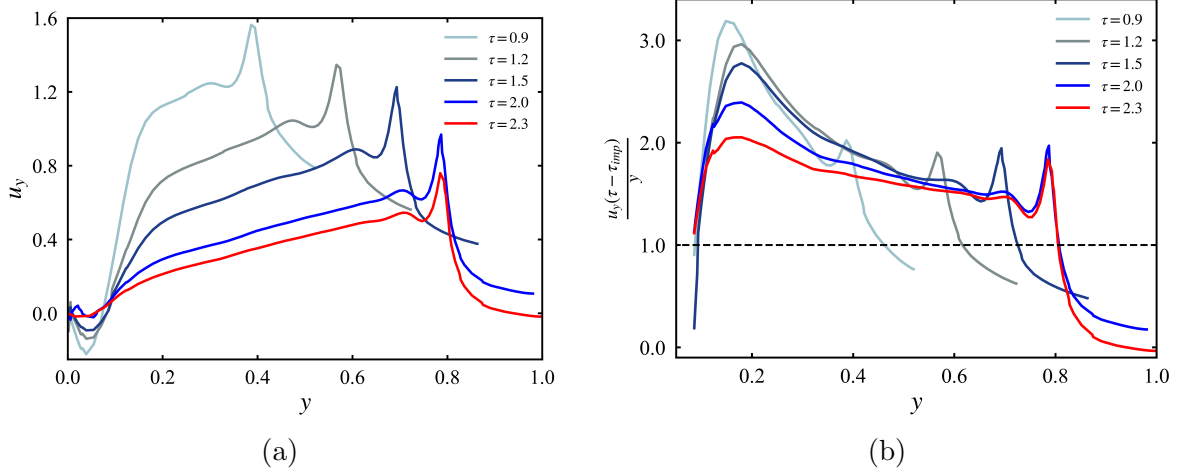


Figure S14: (a) Vertical velocity u_y along the central line of the central sheet over time and (b) rescaled vertical velocity profiles at $We = 130$ and $Re = 1189$

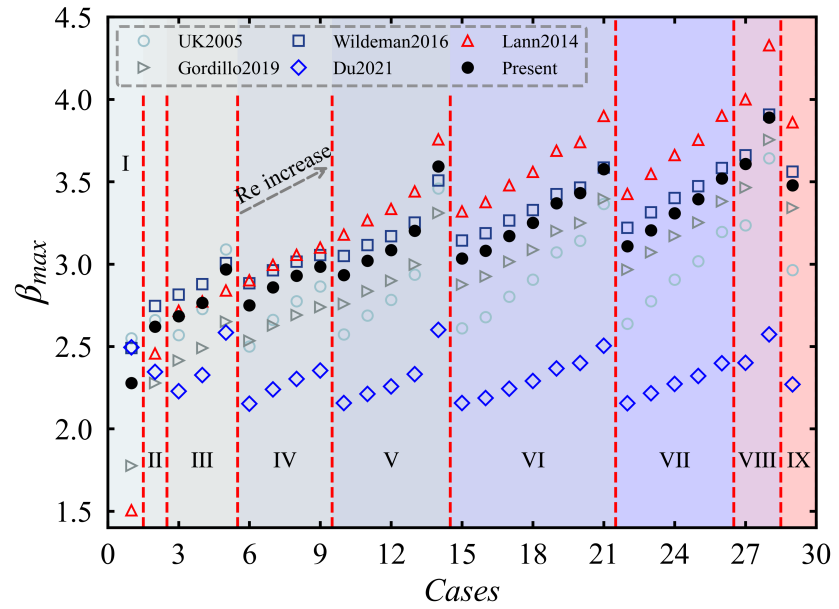


Figure S15: Comparison of maximum spreading radius between simulation results and different models obtained from one drop impact [35–39]. Note: different regimes stand for different We noted by Roman numerals, namely $We = 15$ in I; $We = 30$ in II; $We = 40$ in III; $We = 54$ in IV; $We = 81$ in V; $We = 104$ in VI; $We = 130$ in VII; $We = 150$ in VIII; $We = 200$ in IX, and in each regime Re increases as arrow shows

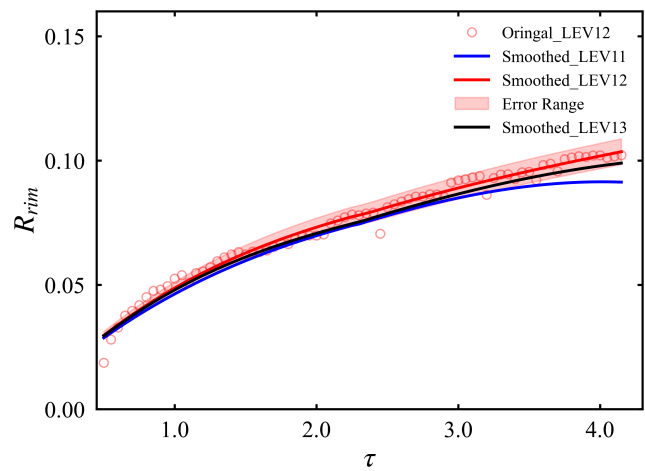


Figure S16: Convergence test of the evolution of R_{rim} on the central sheet for different grid resolution levels at $We = 130$ and $Re = 1189$, with original data shown by hollow symbols and post-processed results by solid lines